King’s Research Portal

*DOI:*
10.1158/2643-3230.BCD-22-0029

*Document Version*
Publisher's PDF, also known as Version of record

Link to publication record in King's Research Portal

*Citation for published version (APA):*
Gargiulo, E., Viry, E., Morande, P. E., Largeot, A., Gonder, S., Xian, F., Ioannou, N., Benzarti, M., Kleine Borgmann, F. B., Mittelbronn, M., Dittmar, G., Nazarov, P. V., Meiser, J., Stamatopoulos, B., Ramsay, A. G., Moussay, E., & Paggetti, J. (2022). Extracellular vesicle secretion by leukemia cells in vivo promotes CLL progression by hampering antitumor T-cell responses. *Blood Cancer Discovery*. https://doi.org/10.1158/2643-3230.BCD-22-0029

**Citing this paper**
Please note that where the full-text provided on King's Research Portal is the Author Accepted Manuscript or Post-Print version this may differ from the final Published version. If citing, it is advised that you check and use the publisher's definitive version for pagination, volume/issue, and date of publication details. And where the final published version is provided on the Research Portal, if citing you are again advised to check the publisher's website for any subsequent corrections.

**General rights**
Copyright and moral rights for the publications made accessible in the Research Portal are retained by the authors and/or other copyright owners and it is a condition of accessing publications that users recognize and abide by the legal requirements associated with these rights.

•Users may download and print one copy of any publication from the Research Portal for the purpose of private study or research.
•You may not further distribute the material or use it for any profit-making activity or commercial gain
•You may freely distribute the URL identifying the publication in the Research Portal

**Take down policy**
If you believe that this document breaches copyright please contact librarypure@kcl.ac.uk providing details, and we will remove access to the work immediately and investigate your claim.

Download date: 08. Oct. 2023

# Extracellular vesicle secretion by leukemia cells *in vivo* promotes CLL progression by hampering antitumor T-cell responses

**Ernesto Gargiulo[1], Elodie Viry[1], Pablo Elías Morande[1,2], Anne Largeot[1], Susanne Gonder[1,3], Feng Xian[4,15], Nikolaos Ioannou[5], Mohaned Benzarti[3,6], Felix Bruno Kleine Borgmann[3,7-8], Michel Mittelbronn[3,8-12], Gunnar Dittmar[3,4], Petr V. Nazarov[13], Johannes Meiser[6], Basile Stamatopoulos[14], Alan G. Ramsay[5], Etienne Moussay[1,]* and Jérôme Paggetti[1,]***

[1] Tumor-Stroma Interactions Group, Department of Cancer Research, Luxembourg Institute of Health, Luxembourg, Luxembourg

[2] Instituto de Medicina Experimental (IMEX)-CONICET- Academia Nacional de Medicina; Buenos Aires, Argentina

[3] Faculty of Science, Technology and Medicine, University of Luxembourg, Esch-sur-Alzette, Luxembourg

[4] Proteomics of Cellular Signaling, Department of Infection and Immunity, Luxembourg Institute of Health, Strassen, Luxembourg

[5] School of Cancer and Pharmaceutical Sciences, Faculty of Life Sciences & Medicine, King's College London, London, United Kingdom

[6] Cancer Metabolism Group, Department of Cancer Research, Luxembourg Institute of Health, Luxembourg, Luxembourg

[7] Department of Neurosurgery, Centre Hospitalier de Luxembourg Luxembourg

[8] Luxembourg Centre of Neuropathology, Department of Cancer Research, Luxembourg Institute of Health, Luxembourg

[9] Luxembourg Centre of Neuropathology, University of Luxembourg, Luxembourg

[10] Department of Life Sciences and Medicine, University of Luxembourg, Esch-sur-Alzette, Luxembourg

[11] National Center of Pathology, Laboratoire national de santé (LNS), Dudelange, Luxembourg

[12] Luxembourg Centre for Systems Biomedicine, University of Luxembourg, Luxembourg

[13] Multiomics Data Science Group, Department of Cancer Research, Luxembourg Institute of Health, Strassen, Luxembourg

[14] Laboratory Of Clinical Cell Therapy, Jules Bordet Institute, Université Libre de Bruxelles, Brussels, Belgium

[15] Present address: Division of Pharmacology & Toxicology, Department of Pharmaceutical Science, University of Vienna, Austria

*****These authors share senior authorship

Correspondence: jerome.paggetti@lih.lu; etienne.moussay@lih.lu; 6 rue Nicolas-Ernest Barblé, L-1210 Luxembourg, Luxembourg, Tel.: +352-26970-344 (J.P.); +352-26970-232 (E.M.)

**Keywords: Small extracellular vesicles, exosomes, CLL, tumor microenvironment, tumor immune escape**

**Short title:** CLL-derived exosomes inhibit antitumor T cells ***in vivo***

**Conflict of Interest:** The authors declare no conflict of interest.

## Abstract

Small extracellular vesicles (sEV, or exosomes) communication among cells in the tumor microenvironment has been modeled mainly in cell culture, while their relevance in cancer pathogenesis and progression *in vivo* is less characterized. Here we investigated cancer-microenvironment interactions in vivo using mouse models of chronic lymphocytic leukemia (CLL). sEV isolated directly from CLL tissue were enriched in specific miRNA and immune checkpoint ligands. Distinct molecular components of tumor-derived sEV altered CD8$^+$ T-cell transcriptome, proteome and metabolome leading to decreased functions and cell exhaustion *ex vivo* and *in vivo*. Using antagomiRs and blocking antibodies, we defined specific cargo-mediated alterations on CD8$^+$ T-cells. Abrogating sEV biogenesis by *Rab27a/b* knockout dramatically delayed CLL pathogenesis. This phenotype was rescued by exogenous leukemic sEV or CD8$^+$ T-cell depletion. Finally, high expression of sEV-related genes correlated with poor outcomes in CLL patients, suggesting sEV profiling as prognostic tool. In conclusion, sEV shape the immune microenvironment during CLL progression.

## Statement of significance

Small extracellular vesicles (sEV) produced in the leukemia microenvironment impair CD8$^+$ T-cell mediated anti-tumor immune response and are indispensable for leukemia progression *in vivo* in murine pre-clinical models. In addition, high expression of sEV-related genes correlated with poor survival and unfavorable clinical parameters in chronic lymphocytic leukemia patients.

## Introduction

Small extracellular vesicles (sEV), or exosomes, are small size particles (30-150 nm) released by every cell and found in any body fluid. They are involved in cell-to-cell communication through the transfer of genetic material and proteins[1], and ligands/receptors interactions, impacting biological functions of target cells[2]. Release of sEV and their cargo depends on the cellular and physiological context[3]. Tumor-derived sEV are involved in the re-education of microenvironment cells promoting tumor proliferation, immune escape and metastasis[4-7].

Survival and proliferation of chronic lymphocytic leukemia (CLL) cells strictly depends on interactions with the microenvironment[8,9]. CLL cells evolve in a highly immuno-suppressive environment[10] where sEV impact progression, invasion and resistance to treatment[7]. We and others previously demonstrated that CLL-derived sEV re-educate surrounding cells and enhance immune escape mechanisms[11-13], such as stromal cell conversion into cancer-associated fibroblasts and modulation of PD-L1 expression on monocytes, among others[14,15].

However, these studies are mostly based on *in vitro* generated sEV. In light of the complex leukemia microenvironment (LME) composition, the role of sEV in CLL pathogenesis *in vivo* still needs to be evaluated. Herein, we developed a protocol to isolate sEV directly from the LME of Eμ-*TCL1* mice with the aim to uncover their complexity and their role in CLL development and progression *in vivo*. We show that sEV isolated from the LME contain specific miRNA and proteins, and display on their surface multiple immune checkpoint (ICP) which play a key role in CLL development, by hampering the anti-tumor CD8$^+$ T-cell-mediated immune response. LME-sEV reprogrammed the CD8$^+$ T-cell transcriptome, proteome and metabolome leading to cell exhaustion, decreased granzyme B production, cytokine secretion and tumor cell lysis. Decrease of sEV secretion by *Rab27* KO led to the impairment of CLL growth *in vivo*. Finally, we showed in a cohort of CLL patients that the expression of genes involved in sEV biogenesis and secretion differs between groups defined by the classical prognosis markers and correlates with survival. Overall, our findings highlight the importance of sEV in the microenvironment for leukemia development and progression.

## Results

### Small EV are enriched in leukemia microenvironment

To assess the relevance of sEV biogenesis in CLL, we performed gene expression analysis using a public dataset[16] comparing CLL patient cells to normal B-cells. We observed higher expression of genes associated with sEV biogenesis in CLL cells (**Fig.1A**), while regulators of retrograde transport and lysosomal degradation were less expressed, resulting in higher computed sEV scores (**Fig.1B**). Furthermore, we observed a higher expression of typical sEV markers, such as the RAB family members and the programmed cell death 6-interacting protein (PDCD6IP, also known as ALIX), associated with increased sEV production (**Fig.1C and Fig.S1A**)[17-19]. This is in accordance with increased levels of CLL-derived sEV (CD20$^+$) in the plasma of CLL patients compared to healthy controls, as we previously reported[15,20]. Interestingly, individual or combined gene expression of major sEV biogenesis regulators, such as *Rab10*, *Rab35*, and *Rab40*c, was higher in cells from patients with unfavorable UM-IGHV than from patients with M-IGHV (**Fig.1D-E and Fig.S1B)**. Similar results were obtained with the Eμ-*TCL1* (TCL1) CLL murine model (GSE175564[21], vs WT B-cells from C57BL/6 mouse, **Fig.1F-G**) as *Cd9*, *Rab3b*, and *Rab31*, were upregulated (**Fig. 1H and Fig.S1C**) in leukemic cells, suggesting an important role of sEV in CLL pathology[18,22,23].

Commonly, sEV are isolated from cell line culture supernatants, allowing to conveniently isolate tumor-derived sEV in large amounts and study their functional impact on accessory cells. However, this method does not fully reflect the complexity of a whole organism. As sEV biogenesis and release are dynamic processes, we aimed to obtain a closer biological representation of sEV from the CLL microenvironment[24].

Therefore, we established a protocol to isolate sEV directly from the spleen of murine models (**Fig.1I**), preserving at the same time cell integrity (**Fig.S1D**). First, we detected a ten-fold enrichment in LME-sEV compared to healthy controls (HCME-sEV, **Fig.1J**). Similarly, we found greater levels of circulating sEV in the peripheral blood (PB) of TCL1 mice compared to healthy controls (**Fig.S1E**), further highlighting sEV potential impact in leukemogenesis.

Overall, isolated ME-sEV showed expected size and morphology (80-120nm, **Fig.1K-L**), presence of typical sEV-markers (**Fig.1M and Fig.S1F**), and the absence of major contaminants for both conditions, validating their use for further downstream analysis. In order to analyze more in-depth the tetraspanin distribution on ME-sEV from both sources, we performed single sEV FC analysis of CD63, CD81 and CD9 (**Fig.1N**). Phenotyping of single-sEV suggests alteration of tetraspanins distribution between LME- and HCME-sEV. Hierarchical clustering further highlighted the heterogeneity of the tetraspanin distribution on single sEV, showing different combinations of CD63, CD9 and CD81 within ME-sEV subsets (**Fig.S1G**). Interestingly, tetraspanin distribution analysis reveals the expansion of distinct LME-sEV subpopulations compared with the healthy counterpart (clusters C1-C10, **Fig.S1H**). These observations, beyond emphasizing the risk of introducing a bias when isolating sEV with single marker-directed beads, highlight the heterogeneity of tumor sEV even on such widely distributed markers.

### LME-sEV present a specific proteome and miRNA fingerprint

While we observed a ten-fold enrichment in sEV in the LME compared to HCME, as well as an alteration of the tetraspanins distribution, we investigated whether their protein and miRNA cargo composition differed. First, a label-free proteomic analysis of equal amounts of proteins derived from LME-sEV and HCME-sEV identified 1,865 proteins with 527 proteins differentially present between groups (**Fig.2A-C**, **TableS1**). Proteins more abundant in LME-sEV (n=281) were involved in translation, RNA splicing and binding, and in the regulation of gene expression and cellular metabolic processes (**Fig.2D**), whereas proteins depleted (n=246) were associated with intracellular transport and with the positive regulation of immune processes, more specifically in lymphocyte activation, migration, and cytokine production (**Fig.2E**), suggesting that LME-sEV may not optimally sustain immune responses but rather stimulate leukemic growth. Given that our proteomic analysis suggested the presence of some conventional (LGALS1 and LGALS9) and metabolic (IL4I1) ICP in LME-sEV (**Fig.2B**), we analyzed the presence of further immune regulatory proteins on ME-sEV surface. Interestingly, LME-sEV carried several ICP ligands, including PD-L1, GAL9, B7-H2, VISTA and MHC I/II (**Fig.2F, Fig.S2A-B**). Furthermore, imaging FC highlighted the co-expression of multiple ICP ligands on CD20$^+$ CLL-derived sEV (**Fig.2G**). The latter was confirmed with single-sEV analysis combined with hierarchical stochastic neighbor embedding (HSNE) clustering, showing PD-L1 and GAL9 often co-expressed on CD20$^+$MHC-II$^+$ vesicles (**Fig.2H-I**), suggesting LME-sEV immuno-suppressive capabilities towards immune cells expressing corresponding receptors. We also observed surface expression of the ectonucleotidases CD39 and CD73, capable to hydrolyze surrounding ATP into adenosine, on LME-sEV (**Fig.S2C**).

We previously reported several miRNA enriched in the plasma of CLL patients (e.g. miR-150 and -155) that correlated with unfavorable clinical parameters[24], and also showed their transfer and functional activity into target cells[14,25]. Therefore, we screened a shortlist of miRNA known to be abundant in CLL and other cancers. Our data showed that murine LME-sEV abundantly carry several miRNA, such as miR-150, -155, -21, -146a, -378a and -27a (**Fig.2J**), typically found in sEV isolated from MEC-1 culture supernatant and patient plasma (**Fig.S2D**)[15]. Although not previously reported in CLL-derived sEV, miR-210, a miRNA associated with hypoxia, was found highly abundant and enriched in LME-sEV, highlighting the dependency of sEV cargo on microenvironment conditions, which are not reflected in cell culture *in vitro*.

## LME-sEV enter different lymphocyte subsets and modify CD8$^+$ T-cells in the microenvironment

As we isolated sEV produced in the spleen, we sought to validate the interaction between these LME-sEV and splenic immune cells. Splenocytes treated *ex vivo* with fluorescent-LME-sEV displayed a rapid and time-dependent internalization which was inhibited by heparin (**Fig.3A-B**), a known inhibitor of sEV uptake[14]. Around 90% of each lymphocyte subsets internalized sEV after 24h (**Fig.3C**). To rule out a possible indirect transfer between splenocytes, we pre-sorted different T cell subsets. Both FC and confocal microscopy confirmed that CD4$^+$ T$_{conv}$ cells, Tregs, and CD8$^+$ T-cells actively internalized LME-sEV *ex vivo*. A total inhibition was observed in presence of heparin highlighting the specificity of the internalization process (**Fig.3D-E**). Injection of fluorescent-ME-sEV in mice led to increased fluorescence in total splenocytes, confirming ME-sEV uptake *in vivo* (**Fig.3F**). In particular, 5 to 10% of T-cells and 40% of B-cells internalized sEV 24h after a single injection (**Fig.3G-H**). Our observations on T-cell subsets contrast with previous studies using *in vitro*-secreted sEV and reporting low internalization[26,27], highlighting the importance of using sEV produced *in vivo* and to study their uptake in a whole organism.

In light of these results, we aimed to evaluate LME-sEV activity on immune surveillance *in vivo*. We injected LME-sEV in Foxp3$^{YFP/Cre}$ mice daily for 7 days, then sorted YFP$^+$-Treg, CD4$^+$ T$_{conv}$, CD8$^+$ T, and CD19$^+$ B-lymphocytes and analyzed gene expression (**Fig.3I-L, Fig.S3, TableS2**). Surprisingly, exclusively CD8$^+$ T-cells showed different expression profiles (**Fig.3I-K, Fig.S3A**) with downregulation of genes involved in immune response (*Cd27*, *Cd226* and *Ms4a4b*) and amino acid transport (*Slc7a5*), while genes associated with inhibition of immune response (*Itpkc*) and T-cell differentiation (*Fgr*) were upregulated (**Fig.3I and 3L**). K-means clustering confirmed the repression of genes regulating immune response and lymphocyte activation (**Fig.S3B**). Ontology analysis also revealed significant changes in crucial biological functions, such as actin cytoskeleton organization (**Fig.3L**, **Fig.S3C**). Similarly, our data showed significant changes in genes associated with oxidoreductase activity, and kinase and phosphatase activities (**Fig.S3C**). Importantly, we could confirm, in a separate *ex vivo* experiment, the rapid decrease in the amino acid transporter *Slc7a5,* and of the co-stimulatory molecules CD27*,* CD96*,* and CD226, crucial for T-cell activation. We also observed the increase in the kinases *Itpkc* and *Fgr* (**Fig.3M-N**), pointing to the negative regulation of cell activation, migration and adhesion. Despite the changes detected in CD8$^+$ T-cells, no significant effect was detected in Tregs, CD4$^+$ T$_{conv}$, and CD19$^+$ B-cells after treating mice *in vivo* (**Fig.S3D-F**). This indicates the selective immunomodulation of CD8$^+$ T-cell compartment, making LME-sEV influence cell-selective rather than systemic. In our experimental setup, CD8$^+$ T-cells appear the principal targets of LME-sEV *in vivo*.

## LME-sEV impact the CD8$^+$ T-cell transcriptome, proteome and metabolome

As LME-sEV alter preferentially CD8$^+$ T-cell *in vivo*, we focused on these essential anti-tumor cytotoxic cells. We profiled gene expression and protein content of sorted CD8$^+$ T lymphocytes treated *ex vivo* with ME-sEV. Only a slight modulation of genes and proteins was observed after 24h (77 genes and 43 proteins, **Fig.S4A-C, TableS1-S2**), all of them involved in lymphocyte activation and immune response (*Itgb1*, *Card6, Tnfrsf4/Ox40*). After 48h, striking changes were observed (331 genes modulated) with the repression of genes involved with CD8$^+$ T-cell activation (*Tlr7*, *Icosl*), survival and proliferation (*Il2, Il2ra*), and immune activity (*Il17a, Lta, Gzmm, Map6*: **Fig.4A-C, TableS2**). In contrast, gene associated with decreased activation and functionality (*Gzmk*), proliferation and survival (*Rora, Il10ra*), and the generation of memory CD8$^+$ T-cells (*Bcl6*) were increased in these cells. The differential transcription factor usage following treatment with LME-sEV suggested an increased differentiation to effector-memory T (T$_{em}$) cells (Zfp281), hyporesponsiveness (Stat1/3 and Myc), and a reduced T cell activation (Snai1/Zeb and Tbr1) (**Fig.S4D**).

In addition, proteomic analysis of LME-sEV-treated CD8$^+$ T-cells showed time-dependent changes in key proteins involved in immune response and metabolism (96h, 422 proteins modulated, **Fig.4D, TableS1**).

Downregulated proteins included the activation marker CD69, and the serine protease granzyme B (GzmB), both crucial for CD8$^+$ T-cell effector functions. Repression of both cytolytic effector molecules GzmB and perforin was also independently confirmed (**Fig.4E-F**). Analysis of proteomics data with a miRNA-target prediction algorithm indicated that a significant fraction of proteins repressed by LME-sEV are putative targets of at least a specific miRNA found enriched in LME-sEV (**Fig.S4E, Fig.2J**). This suggests an active protein downregulation mediated by miRNA transferred by LME-sEV into CD8$^+$ T-cells.

Functionally, proteins increased were involved in gene expression, RNA processing, and translation while proteins repressed were linked to metabolism (**Fig.4G-H**). Interestingly, the amino acid transporter Slc1a5 and the glutamate cysteine ligase (Gclc) were affected, the latter being essential for fueling CD8$^+$ lymphocytes after activation[28]. Conversely, we observed accumulation of the inhibitory pyruvate dehydrogenase phosphatase regulatory subunit (PDPR, **Fig.4D**). To validate these observations, we performed metabolic profiling on ME-sEV treated CD8$^+$ T-cells. By analyzing the uptake/release rates from cell culture medium, an increased consumption of glucose and glutamine, as well as increased lactate release rate suggested a rewiring of central carbon metabolism (**Fig.4I and S4F**). Enhanced glycolysis was also highlighted by the increase of glycolysis-related proteins, including glucose transporter 1 (GLUT1) and D-3-phosphoglycerate dehydrogenase (PHGDH) (**Fig.4J**). However, isotopologue tracing demonstrated that the contribution of glucose to nucleotide *de novo* synthesis, via the pentose phosphate pathway (PPP), was considerably reduced (**Fig.4K and S4G**) indicating a decreased proliferative potential. Based on the results derived from $^{13}$C-Glucose tracing, we hypothesized that an increased consumption of glutamine would lead to an increased usage in the tricarboxylic acid (TCA) cycle. Interestingly, the relative flux of glutamine towards TCA metabolites, proline and glutathione (GSH) was not different after LME-sEV treatment (**Fig.S4H**). Throughout the TCA cycle, molecules of NADH (nicotinamide adenine dinucleotide (NAD) + hydrogen (H)) is generated. Oxygen is particularly important to oxidize NADH to NAD$^+$ used to generate ATP and perform multiple biological processes. However, using seahorse analysis, we observed a decreased oxygen consumption rate (OCR) in the presence of LME-sEV (**Fig.4L**). These data demonstrated that CD8$^+$ T-cells have decreased oxidative phosphorylation potential when treated with LME-sEV. Finally, the use of glutamine for protein synthesis is in accordance with our observation that translation is highly increased in CD8$^+$ T-cells treated with LME-sEV (**Fig.4H**). Glutamine is also used for purine and pyrimidine bases synthesis. Indeed, higher levels of metabolites, including ADP and ATP, were found in CD8$^+$ T-cells treated with LME-sEV (**Fig.S4I**). Altogether, our data suggest LME-sEV-mediated profound perturbations in CD8$^+$ T-cells leading to metabolic blockade (**Fig.S4J**). Accordingly, increased glycolysis was recently linked with CD8$^+$ T-cell exhaustion[29].

Finally, CD8$^+$ T-cell functions are tightly regulated by other immune cells, in particular other lymphocytes subsets. Despite the injection of LME-sEV *in vivo* didn't show considerable effect on other lymphocytes than CD8$^+$ T-cells (**Fig. S3D-F**), we cannot rule out that a direct exposure to sEV in the LME could lead to substantial impact on these cells. Thus, we exposed Tregs, CD4$^+$ T$_{conv}$ cells, and CD19$^+$ B-cells to purified ME-sEV *ex vivo* and inspected gene expression. We identified 378 genes regulated in Treg pointing to an activated phenotype[30] (TNFRSF9$^+$, **Fig.S5A-C, TableS2**). Effector molecules (*GzmB* and *GzmK)*, signaling molecules (*Stat1, Irf4, Irak3)*, and activation markers (*Pdcd1*, *Cd27*, *Tigit)* were increased. We also confirmed an increase of GzmB at protein level (**Fig.S5D**). Interestingly, the majority of DEGs were repressed by LME-sEV in CD4$^+$ T$_{conv}$ cells (211 out of 227, *Cd27, Il7r, Il17ra, Tcf7, Tox*) indicating a strong suppression of T-cell activation and proliferation (**Fig.S5E-G, TableS2**). CD19$^+$ B-cells were the least affected (77 DEGs and no enriched ontology, **Fig.S5H-I, TableS2**).

Altogether, these data indicate that CD8$^+$ T-cells are major targets of LME-sEV *in vivo* and *ex vivo* as transcriptomic, proteomic and metabolic evaluations pointed to profound perturbations of cell activation, proliferation, and immune functions. Worth of notice, *ex vivo* LME-sEV-treated Treg showed a highly suppressive phenotype that could contribute to $CD8^+$ T-cell repression in the tumor microenvironment.

## LME-sEV decrease $CD8^+$ T-cell functions

First, we screened splenic $CD3^+$ vs $CD3^-$ cells from leukemic mice for the expression of ICP receptors and found an enrichment of a variety of ICP receptors in $CD3^+$ T-cells (**Fig.S6A**), confirming the highly exhausted and immunosuppressive microenvironment we previously reported in TCL1 mice[10]. Next, we evaluated the phenotype and activity of $CD8^+$ T-cells treated with LME-sEV. First, LME-sEV stimulated the generation of $CD8^+$ lymphocytes sub-populations, as visible by the expansion of $T_{em}$ cells (**Fig.5A-B**). We performed a clustering of $CD8^+$ T-cells based on ICP surface expression, using HSNE algorithm. Eleven clusters were identified based on ICOS, LAG3, PD1, TIGIT, and TIM3 expression among $T_{em}$ cells (**Fig.5C-D**). Clusters C1 and C8 co-expressing the 5 ICP were significantly enriched (**Fig.5E**), suggesting an exhausted phenotype. Concerning sEV immuno-modulatory effects, IL-2 and IFN-γ synthesis was particularly decreased by LME-sEV, demonstrating their impact on $CD8^+$ lymphocyte cytokine polyfunctionality (**Fig.S6B-D**). In addition, adenosine, converted by CD39/CD73 starting from ATP, significantly reduces $CD8^+$ T-cells proliferative capacity[31]. Indeed, proliferation of $CD8^+$ T-cells is markedly reduced by LME-sEV (expressing CD39, **Fig.S2C**) treatment in presence of ATP (**Fig.S6E**). This, together with the decrease in perforin and GzmB (**Fig.4F**), strongly suggests a robust LME-sEV-mediated deregulation of $CD8^+$ T-cell signaling and production of cytokines and cytotoxic molecules.

Therefore, we aimed to confirm the functional impact of LME-sEV on $CD8^+$ T-cells using an *ex vivo* quantitative cytotoxicity assay against TCL1 CLL cells. LME-sEV treatment led to reduced cytotoxic activity of $CD8^+$ T-cells against CLL cells (**Fig.5F**), without altering the ability of $CD8^+$ lymphocytes to interact with target cells (**Fig.5G**). Importantly, LME-sEV decreased the ability of $CD8^+$ T-cells to form F actin-enriched immune synapses, a key signaling structure required to drive the secretion of cytolytic granules to lytic synapses (**Fig.5H**). Consistent with decreased RNA and protein levels (**Fig.4E-F**), the level of GzmB expression at the synapse was markedly reduced in $CD8^+$ T-cells treated with LME-sEV (**Fig.5I**). In accordance with the enrichment of LME-sEV in several miRNAs (**Fig.2J**), we observed a significant increase in miRNA levels in $CD8^+$ T-cells treated with LME-sEV (**Fig.5J, Fig.S6F**). Interestingly, these miRNAs (miR-150, -155 and -378a ) were previously described as negative regulators of GmzB in $CD8^+$ T and NK cells[32-35], two markers that we found recurrently downregulated in $CD8^+$ lymphocytes treated with LME-sEV (**Fig.4D-F, Fig.5I**).

To identify particular cargoes responsible for the effects observed on $CD8^+$ T cells, we focused on these miRNAs as they are transferred to target cells as well as on ICP as highly important regulators of T cell functions.

Treated $CD8^+$ T-cells with LME-sEV previously transfected with antagomiRs targeting miR-150, -155, and -378a, showed a rescue in GzmB and CD226 protein levels, comparable to $CD8^+$ T-cells treated with HCME-sEV or LME-sEV pre-coated with heparin (**Fig.5K**), while Prf1 and Itpkc levels remained unaffected (**Fig.S6G**). In addition, the transfection of LME-sEV with single antagomiRs did not restore the levels of target genes in treated $CD8^+$ T-cells (**Fig.S6H**), demonstrating that multiple miRNAs are needed to target these molecules. Interestingly, treatment with HCME-sEV transfected with miRNA mimics for miR-150, -155, and -378a had a similar effect on GzmB level than LME-sEV, confirming that the repression of GzmB we observed was due to these miRNAs (**Fig.S6I**).

Next, we focused on ICP ligands present on LME-sEV surface and used blocking antibodies to neutralize their immunosuppressive functions on $CD8^+$ T-cells. While LME-sEV (+ isotype Ab) stimulated ICP expression and decreased GzmB and perforin levels as we previously showed, pre-incubation with anti-PD-L1, GAL9, VISTA and MHC-II blocking Ab decreased ICP expression, restored perforin level, but had no effect on GzmB level in treated CD8$^+$ T-cells (**Fig.5L**), suggesting that different molecules present in LME-sEV affect multiple pathways in target cells leading to their overall effect.

Altogether, through multiple molecules, LME-sEV decreased CD8$^+$ T-cell functional potential, impacting cytokine production and engaging ICP receptors, thus decreasing cytotoxic effect towards tumor cells.

**Small EV are crucial for CLL development by impairing the anti-tumor immune response *in vivo***

Considering the enrichment of sEV in the LME, their specific cargo and surface molecules, and impact on CD8$^+$ T-cells, we investigated their role during CLL development *in vivo,* by genetically impairing sEV release in a novel preclinical CLL murine model, TCL1-RAB27DKO (**Fig.6A**). RAB27A and B are two proteins essential for sEV release, being majorly involved in the docking of vesicles at the cellular membrane[36-38]. Validation of the model showed presence of the human *TCL1* transgene together with the *Rab27b* genomic deletion, and lack of both RAB27A and B proteins (**Fig.6B-C**). TCL1-RAB27DKO showed a striking delay in CLL progression, noticeable by the slower accumulation of CD5$^+$CD19$^+$ CLL cells in the PB, and consequent increased mouse survival (**Fig.6D-E**), further confirmed with histological analyses of the spleens (**Fig.S7A**). TCL1-RAB27DKO ultimately developed the disease and required euthanasia. Despite TCL1-RAB27DKO spleens were of comparable size as TCL1, the quantity of LME-sEV was dramatically decreased (**Fig.6F**, **Fig.S7B**). In addition, LME-sEV$_{\text{TCL1-RAB27DKO}}$ protein content is largely different (546 proteins modulated, **Fig.6G-H, Fig.S7C, TableS1**). Indeed, LME-sEV$_{\text{TCL1-RAB27DKO}}$ contained lower quantity of several proteins involved in the suppression and control of lymphocyte activation, signaling and proliferation (LGASL1, LGASL9, CXCR5, IL4I1, BLK, SYK) whereas proteins enriched were involved in gene expression, RNA processing and translation (**Fig.6H**, **Fig.S7D-E**). Based on the differentially present proteins, sEV preparations clustered in PCA according to mouse genotypes (**Fig.S7F**).

Next, we compared gene expression from TCL1-RAB27DKO and TCL1 leukemic cells (**Fig.S7G-H, TableS2**). GSEA confirmed the decrease, at mRNA level, of protein secretion in TCL1-RAB27DKO cells (**Fig.S7I**). Rab27 inactivation led to decreased expression of genes involved in vesicle trafficking (*Bet1, Lamp2, Rab7, Scamp1, Vamp1*) while *Snx31* responsible for vesicles formation in the MVB was upregulated (**Fig.S7G)**. Interestingly, an enrichment in genesets driven by NF-κB, Myc, and Wnt/β-catenin was observed, suggesting the induction of oncogenic programs as compensatory mechanism (**Fig.S7I**).

To confirm that the delay in CLL development was due to CLL cell inability to release sEV, rather than to a general lack of sEV in the LME, we transferred CLL cells isolated from spleens of TCL1 or TCL1-RAB27DKO mice into WT C57BL/6 recipient mice. Contrary to TCL1 cells, TCL1-RAB27DKO cells failed to recapitulate CLL development (**Fig.6I-J**, **Fig.S8A**). Importantly, injection of LME-sEV rescued leukemia development to levels comparable to TCL1 transfer, demonstrating the impact of LME-sEV on CLL development **(Fig.6I-J, Fig.S8A)**. To evaluate a potential autocrine effect, we treated *ex vivo* TCL1-RAB27DKO leukemic cells with LME-sEV or LME-sEV$_{\text{TCL1-RAB27DKO}}$ (**Fig.S8B-D**, **TableS2**). The effect was moderate and pointed to B-cell functions (*Bach2* and *Maf*) and increased immunosuppressive capabilities (*Cx3cr1*).

Despite being unable to recapitulate the disease in immunocompetent C57BL/6 mice, TCL1-RAB27DKO CLL cells successfully induced leukemia development in immunodeficient NSG mice (**Fig.S8E-H**), highlighting the proficiency of TCL1-RAB27DKO CLL cells to engraft when the immune system is not intact. To confirm that CD8$^+$ T-cells are key in the control of CLL development, we selectively depleted CD8$^+$ T-cells in C57BL/6 mice before injecting TCL1-RAB27DKO CLL cells (**Fig.6K, Fig.S8I**). We observed a rapid increase of percentage and number of leukemic cells in the blood and spleen of CD8$^+$-depleted mice (**Fig.6L, Fig.S8J-K**), endorsing the role of CD8$^+$ T-cell-mediated immune surveillance of TCL1-RAB27DKO CLL cells. In a final experiment, we sought to evaluate *in vivo* the ability of ME-sEV to affect CD8$^+$ T-cells and therefore to influence disease outcome (**Fig.6M**). Mice depleted in endogenous CD8$^+$ T-cells and injected with TCL1-RAB27DKO CLL cells, had significantly more CLL cells in the PB and shorter survival when injected with CD8$^+$ T-cells previously treated with LME-sEV compared with HCME-sEV (**Fig. 6N-O**). We also observed that LME-sEV-treated CD8$^+$

T-cells did neither persist nor proliferate in recipient mice, possibly explaining the different outcomes (**Fig.S8L-M**).

Altogether, we demonstrated here that TCL1-RAB27DKO CLL cells fail to induce CLL in C57BL/6 due to their inability to release sEV and impact the microenvironment. LME-sEV inhibit CD8$^+$ T-cells-mediated anti-tumor immunity and are sufficient to restore the leukemic potential of TCL1-RAB27DKO CLL cells.

**Expression of sEV-related genes correlates with disease progression and poor survival in CLL patients**

To validate the importance of sEV in CLL patients, we quantified the expression of *RAB7a, RAB10, RAB27a, RAB31, RAB35, RAB40C* and *PDCD6lP*, involved in vesicle biogenesis and secretion by RT-qPCR in a cohort of 144 CLL patients. We identified *RAB27a* and *RAB31* as predictors of OS, as higher expression correlated with poor OS (**Fig.7A-B**, **Fig.S9A**). Similarly, when combining *RAB27a* and *RAB31* with other sEV-related genes, the signature correlated with OS (**Fig. 7C**) and higher hazard ratio (HR, **Fig.7D**). Similar results were obtained for TFS (**Fig.7E-F**, **Fig.S9B-D**). Single-gene analysis confirmed the differential expression of *RAB7a, RAB27a, RAB31,* and *RAB35* between CLL groups (e.g. ZAP70$^+$ vs ZAP70$^-$) and sub-groups (e.g. IGHV$_M$ LPL$^+$ vs IGHV$_{UM}$ LPL$^-$, **Fig.7G**, **Fig.S9E**) characterized by the expression of markers classifiers of prognosis. Similarly, we identified signatures differentially expressed between clinical groups (**Fig.7H**). Altogether, our data confirmed the relevance of sEV in CLL pathology.

## Discussion

Recent studies focused on understanding how the microenvironment sustains tumor growth and protects cancer cells. In this regard, sEV are important for cell-to-cell communication, and thus represent possible targets for anti-tumor therapies. The complexity behind sEV-based communication during cancer development relies on their ability to alter the microenvironment cellular composition and functions. Previous works by us and others partially elucidated sEV involvement in CLL progression and remodeling of the TME[5,13-15]. Interestingly, we found here a sEV-signature linked with the biogenesis and release of sEV by CLL cells in human and mice. However, the relevance of such studies using cell line- or plasma-derived sEV and *in vitro* cultures, points to the need of more physiological conditions to study sEV[24]. This confirmed the relevance of designing a robust protocol to isolate sEV from the murine LME. We focused our attention on the functional effect of LME-sEV on lymphocyte subsets as they internalized LME-sEV, highlighting the possibility of cargo-mediated effects in addition to surface molecule interactions. T-lymphocytes are known to poorly internalize sEV[26,27]. This discrepancy suggests the presence of surface molecules on sEV produced in a whole organism that could lack when produced *in vitro*. Importantly, we noted that exclusively CD8$^+$ T-cells were affected after seven days of treatment *in vivo*. This unforeseen observation indicated a certain specificity of sEV rather than a broad effect, as LME-sEV could enter multiple lymphocyte subsets *in vitro*. Again, this highlights the need of a whole microenvironment to fully understand the role of sEV in cancer[24].

We characterized LME-sEV to decipher their impact on the TME. Surface molecules screening highlighted the enrichment in CD20 on LME-sEV, confirming the B-cell origin of the vesicles and our previous observation[14]. PD-L1, CTLA-4, and TIM-3 were already reported as crucial effectors of sEV function on immune cells[39]. Given the complexity of sEV content, we believe that sEV convey molecules of multiple natures (ICP, miRNA, enzymes) having complementary functions. First, we found multiple ICP ligands on LME-sEV, and the corresponding receptors on matched spleens CD3$^+$ T-cells. This supports our previous report of multiple ICP receptors on T-cells in murine CLL[10], the possible engagement of ligands carried by sEV inducing T-cell exhaustion and immune escape[7]. Moreover, the presence of multiple miRNAs enriched in CLL-sEV[15,25,40,41], transferred to CD8$^+$ T-cells, and known to disrupt effector cell cytotoxic properties[32-35] pointed to GzmB and perforin, consistently inhibited by LME-sEV in CD8$^+$ T-cells. miRNA neutralization and ICP blockade both partially reversed the effects observed on CD8$^+$ T-cells. As a functional readout, we also focused on immune synapse formation between CD8$^+$ T-cells and TCL1 leukemic B-cells, and confirmed reduced expression of GzmB at lytic synapses in CD8$^+$ T-cells previously exposed to LME-sEV *in vitro*, ultimately leading to decreased functional cytotoxicity. Interestingly, LME-sEV had an opposite effect on Treg, stimulating the expression of GzmB, and thus their immunosuppressive functions[42]. We confirmed that treatment of CD8$^+$ T-cells with ATP and CD39$^+$LME-sEV decreased proliferation, cytotoxicity and IL-2/GzmB production[31,43]. Overall, the combinatory activity of ICP, miRNAs and hydrolytic enzymes leads to a decrease in T-cell functionalities, ultimately suppressing the anti-tumor immune response. In accordance with this, gene expression profiling from *in vitro* and *in vivo* LME-sEV-treated CD8$^+$ T-cells further showed a consistent impact on immune functions, cytokine release, cytoskeleton organization, as well as metabolic changes. Metabolic adaptation and manipulation by the tumor is recognized as a hallmark of cancer. Recently, tumor-derived EV were shown to reprogram the metabolism of macrophages thereby preparing an immuno-suppressive niche characterized by increased glycolysis and lactate release[44]. These metabolic adaptations - increased glucose consumption and lactate release - are known markers of exhaustion[29] that we also observed in LME-sEV-treated CD8$^+$ T-cells. The TCA cycle produces energy to feed the oxidative phosphorylation (OXPHOS). Recently, a high OXPHOS in CD8$^+$ T-cells was described to be deleterious for immunotherapy in melanoma[45]. In addition, we identified inside LME-sEV proteins involved in metabolism, including IL4I1, a metabolic ICP recently described in CLL[46], also pointing to the possible delivery of the enzyme to immune cells, thus influencing their activation status. Finally, although no striking effect of LME-sEV on Treg was observed *in vivo*, the vesicles rapidly modified Treg *in vitro* towards a more immuno-suppressive phenotype similar to the one observed in TCL1 mice. Their activation and GzmB increase *in vitro* confirmed their potential to respond to LME-sEV and suggested their involvement in the long-term hindered T-cell response *in vivo*.

To confirm the crucial role of sEV *in vivo*, we generated TCL1-RAB27DKO model in which sEV release is inhibited[47]. Although Rab27DKO mice are partially immunodeficient[48], secretion of cytokines by Rab27DKO immune cells remains unaffected[49]. TCL1-RAB27DKO CLL cells showed strong NFκB- and Myc-driven oncogenic transcriptional programs, and grew in immunodeficient mice. However, we noted a striking delay of disease onset in mice deprived of sEV, and TCL1-RAB27DKO CLL cells transfer of into immunocompetent mice failed to recapitulate the disease. Importantly, the reintroduction of LME-sEV rescued leukemia development. We also showed, by a depletion experiment, that CD8$^+$ T-cells are crucial for controlling CLL development in absence of sEV. Finally, we confirmed that LME-sEV are impairing T cell functions as leukemic mice adoptively transferred with CD8$^+$ T-cells activated in presence of LME-sEV had a shorter survival than with HCME-sEV. Altogether, despite sEV-deficient CLL cells were fit to grow *in vivo*, sEV are indispensable to escape the anti-tumor immune response in immunocompetent animals.

Finally, using a cohort of CLL patients, we found a correlation between sEV-related gene expression, prognostic markers, and survival. Enhanced expression of *RAB27A* gene by breast cancer cells promotes invasiveness and metastasis potential[50], suggesting a crucial role for sEV in aggressive malignancies. In conclusion, we stressed on the importance to focus and characterize more complex sources of sEV, and not limiting our evaluations on sEV produced *in vitro*. Current therapies using ICP blockers showed a limited effect against CLL, with benefit for patients with Richter transformation[51]. Having a broader overview of the TME, including sEV composition, could be key to better understand cancer progression and resistance to establish effective therapeutic strategies for patients[52].

## Methods

### Patient samples

All experiments involving human samples were conducted in accordance with the declaration of Helsinki, approved by the institutional review board (Jules Bordet Institute Ethics Committee) and peripheral blood samples were collected from treatment-naïve CLL patients after written informed consent. Patient cohort demographic characteristics (age and gender) and clinical parameters (Binet stage, IgHV status, zeta-associated protein 70 (ZAP70), lipoprotein lipase (LPL), CD38 molecule (CD38) expression, cytogenetic abnormalities, lymphocyte doubling time (LDT), and soluble CD23 (sCD23) are derived from our previous reports[53,54] and reported in **TableS3**. All patients had a CD19$^+$CD5$^+$CD23$^+$ phenotype and a Catovsky score of 4/5 or 5/5. All tested prognostic factors were proven to be significant predictors of treatment-free survival (TFS) and overall survival (OS), indicating that our cohort is representative of a CLL population.

### Animal experiments

All experiments involving laboratory animals were conducted in a pathogen-free animal facility with the approval of the Luxembourg Ministry for Agriculture (#LECR-2016-03, #LECR-2018-02 and #LECR-2018-03). Mice were treated in accordance with the European Union guidelines. C57BL/6 mice (MGI:3028467, RRID:IMSR_JAX:000664) were purchased from Janvier Labs (France) and NSG (MGI:3577020, RRID:IMSR_JAX:005557) mice and Foxp3$^{YFP/Cre}$ (MGI:3790499, RRID:IMSR_JAX:016959) from Jackson Laboratories (USA). Eμ-*TCL1* mice (on C57BL/6 background; MGI:3527221) were a kind gift from Pr. Carlo Croce and Pr. John Byrd (OSU, OH) and provided by Dr. Martina Seiffert (DKFZ Heidelberg, Germany). The *Rab27a*$^{ash/ash}$ (MGI:1856656) *Rab27b*$^{-/-}$ (MGI:3834149; RAB27DKO) were previously described[47]. Eμ-*TCL1 Rab27a*$^{ash/ash}$ *Rab27b*$^{-/-}$ (called TCL1-RAB27DKO) mice were generated in-house as depicted in **Fig.6A.** by crossing the RAB27DKO with TCL1, to introduce the TCL1 oncogene, generating the Eμ-*TCL1 Rab27a*$^{ash/+}$ *Rab27b*$^{-/+}$. Further breeding with the RAB27DKO mice established the Eμ-*TCL1 Rab27a*$^{ash/ash}$ *Rab27b*$^{-/-}$. CLL progression was monitored over several months in TCL1 and TCL1-RAB27DKO by determining the percentage of CD5$^+$CD19$^+$ CLL cells in PBMC by flow cytometry on a Cytoflex (Beckman Coulter, USA) using CD19-APC and CD5-PE (Biolegend, USA). Mice reaching the humane endpoint were euthanized by cervical dislocation. All deaths unrelated to leukemia were excluded from this study. To perform adoptive transfer (AT) in C57BL/6 and NSG control mice, CLL cells were isolated from either TCL1 or TCL1-RAB27DKO diseased spleens. Then, 10 x 10$^6$ CLL cells were injected intravenously in 100 µL of DMEM without phenol red, and CLL progression was followed by weekly bleeding, as described previously. Otherwise stated, mice used for experiments were eight to ten weeks old. Both male and female mice were used (age and gender were matched within the same experiment), no variation or impact on the results due to the different sex was detected.

### Validation of the TCL1-RAB27DKO mouse model

Genomic DNA was extracted from a tail biopsy using Mouse Direct PCR Kit (#B40015, Biotool) following the manufacturer's instructions. The specific primer sequences were: for *Tcl1* F: 5'-GCCGAGTGCCCGACACTC-3' and R: 5'-CATCTGGCAGCAGCTCGA-3', for *Rab27b* F: 5'-CTGCTGCAGGATCTCACATCAGTG-3', $R_1$: 5'-AGCATCTGTAACCTAGACATTGGC-3' and $R_2$: 5'-GAAATGGGACATTGGGACAGGAGG-3'. Both amplifications were performed with the following program: 94°C for 5 min, 35 cycles of 94°C for 20 seconds, 59°C for 30 seconds, and 72°C for 60 seconds. After amplification, the product was run on a 1% agarose gel with SYBR™ Safe DNA Gel Stain (ThermoFisher, Waltham, MA, USA) and visualized by Image Quant Las 4000 (GE Healthcare, Chicago, IL, USA).

Proteins from freshly isolated cells (total blood) were extracted using RIPA buffer including the cOmplete™ Protease Inhibitor Cocktail (Roche, Basel, Switzerland) and the Phosphatase Inhibitor Cocktail 2 and 3 (Sigma-Aldrich, Burlington, MA, USA). Then, 10µg of cell lysates were resolved on 10% SDS-PAGE and transferred to a nitrocellulose membrane. To confirm equivalent loading between lanes, a Ponceau red staining was performed. Membranes were incubated in 1xPBS-0.1%Tween and fat-free dry milk (5%, Roth) blocking buffer during 1h at RT. Membranes were then incubated with primary antibodies against RAB27a (#sc-81914, RRID:AB_1128884, Santa Cruz), RAB27b (#NBP1-79631, RRID:AB_11014614, Novus) and HSC70

(#sc-7298, RRID:AB_627761, Santa Cruz) in blocking buffer at 4°C overnight. Membranes were washed three times in 1xPBS-0.1%Tween for 10 min each time. Secondary antibodies coupled to HRP were from Jackson ImmunoResearch. For detection, the ECL western blot detection kit was purchased from Amersham, and the radiographic films from Santa Cruz Biotechnology.

### *In vivo* depletion of $CD8^+$ T cells

TCL1-RAB27DKO cells ($20*10^6$/mouse) were injected (i.v.) in C57BL/6 mice treated with 200µg (day -2, 0 and 3) and 100µg (weekly) of either blocking ab against CD8 (InVivoMAb anti-mouse CD8α, #BE0061, RRID:AB_1125541, Bioxcell) or isotype control (InVivoMAb polyclonal Armenian hamster IgG, #BE0091, RRID:AB_1107773, Bioxcell) as showed in **Fig.6K**.

For $CD8^+$ T-cell transfer experiment, TCL1-RAB27DKO cells ($5*10^6$/mouse) were injected i.v. (tail vein) in C57BL/6 mice treated with 100µg (day -1 and 0) of anti-CD8 blocking Ab as showed in **Fig.6M**. At day 7, $2*10^6$ *ex vivo* ME-sEV-treated $CD8^+$ T-cells were injected i.p. in each mouse.

### ME-sEV isolation

To isolate LME-sEV, we used spleens from animals with over 70% $CD5^+CD19^+$ cells in PB. Dissociation was performed using GentleMACS™ (Miltenyi). The protocol derives from previous publications with modifications[14,55] and is depicted in **Fig.1I**. Dissociated spleens were centrifuged for 5 min at 400g, allowing to collect cells for downstream analysis and supernatant, called spleen plasma. Spleen plasma was centrifuged for 20 min at 400g to remove remaining cells, 40 min at 2,000g to remove dead cells and 60 min at 10,000g to remove cellular debris and large EV. Before ultracentrifugation (UC), the spleen plasma was filtered (0.22µm) to remove any impurity. Small EV were isolated by UC (70 min, 110,000g, 4°C) followed by floatation on 17% iodixanol cushion (Optiprep, Axis-Shield, 75 min, 100,000g, 4°C) to remove protein complexes. Finally, sEV were washed in PBS (70 min, 110,000g, 4°C). To remove aggregates, we filtered sEV at 0.45µm followed by 0.22µm. To prepare fluorescent sEV, vesicles were incubated with MemBright (now called MemGlow™) 488 or 570 dyes (200nM)[56] for 15 min at 4°C before being loaded on 17% iodixanol cushion and further processed with standard protocol. To preserve sEV integrity, each preparation was divided in aliquots and kept at -80°C until further use. Quantification of sEV-associated proteins was performed as previously described[55]. Briefly, 4.5µl of fresh isolated sEV were lysed in 0.5µl of 10X RIPA buffer and 2µl of the mix was measured via spectrophotometer (595nm) using 1ml of Bradford reagent (BIO-RAD). Protein concentration was determined using a BSA standard curve.

### ME-sEV size analysis

Tunable resisting pulse sensing (TRPS) was performed with Exoid (Izon Science) using a NP100 nanopore (100nm) and PBS buffer as electrolyte. Data were analyzed using the provided Izon Control Suite software (RRID:SCR_021922).

### Detection of sEV markers by western blot

Details for sEV western blot were previously described[55]. To assess sEV purity, the presence of the following markers was assessed: Alix (i.e. PDCD6IP, #2171, RRID:AB_2299455, Signaling Technology), TSG101 (#GTX70255, RRID:AB_373239, GeneTex), CD63 (#556019, RRID:AB_396297, BD Biosciences), CD81 (#sc-7637, RRID:AB_627190, Santa Cruz Biotechnology). Furthermore, the absence of two common contaminating proteins Calnexin (#2433, RRID:AB_2243887, Cell Signaling Technology) and PHB (#sc-377037, RRID:AB_2714190, Santa Cruz Biotechnology) was also evaluated.

### Electron microscopy

Small EV analysis was performed using formvar- and carbon-coated (ultra-thin, 200 mesh, EMS 215-412-8400) copper grids in a Cressington 208 glow-discharge unit before applying 1µl of sample (diluted in different concentrations in $H_2O$) per grid. The grids were then washed in $H_2O$ three times and stained with uranylacetate for negative contrast. Imaging was taken with a Gemini SEM 300 (Zeiss, Oberkochen, Germany) at 30kV acceleration voltage using the sTEM detector.

**Flow cytometry analysis of sEV**

*Conventional flow cytometry (Bead-based strategy)*

Small EV were coated on beads as previously published[57]. Briefly, 4µm aldehyde/sulfate latex beads were coated with 5µg of ME-sEV by incubating them ON at 4°C. Saturation of remaining free binding sites was done using 1M glycine. Beads were then washed 4 times in PBS/0.5% BSA (3 min 4,000g RT). Finally, 10µl of ME-sEV coated beads were incubated with 50µl of antibody diluted in PBS/0.5% BSA (30 min at 4°C). After two washes, sEV-coated beads were analyzed with the CytoFLEX flow cytometer (Beckman Coulter; RRID:SCR_019627). The full list of antibodies used for sEV staining can be found in **TableS4**.

*Conventional flow cytometry (Bead-free single-EV strategy)*

Prior to the staining, antibodies and PBS were filtered through a 0.22µm filter. $MB488^+$ sEV were then stained with antibodies for 30 min at 4°C. Acquisition was performed with NovoCyte Quanteon Flow Cytometer (Agilent) equipped with 0.22µm filter for the sheath fluid to reduce electronic noise. Furthermore, the instrument was set to minimum flow rate (5µl/min).

*Imaging flow cytometry (Bead-free single-EV strategy)*

$MB488^+$ sEV were stained with antibodies for 30 min at RT, resuspended in PBS up to 200µl, filtered (0.22µm) and incubated at 4°C ON before acquisition with the ImageStream®X Mark II imaging flow cytometer (EMD Millipore). Stained $MB488^+$ sEV were acquired by setting the imaging flow cytometer as previously published[57]. Briefly, the instrument was set to low speed/high sensitivity mode (60x magnification) and the power for the used lasers was set to the maximum.

***In vitro* uptake of sEV**

Cells were seeded on glass coverslips in µ-slides (Ibidi, Germany). Then, MB488 fluorescently labelled LME-sEV were used to treat the cells for the desired time-points. Heparin (Hep) was used as uptake inhibitor, in this case the labeled sEV were incubated 30 min at 37°C with 10ng/ml heparin (Sigma-Aldrich) prior treating the cells[14].

*Flow cytometry analysis*

At the time of collection, cells were washed in MACS buffer (Miltenyi Biotec). Cell surface staining was performed in 100µl of MACS buffer (Miltenyi Biotec) for 30 min on ice in the dark prior analysis on the CytoFLEX (Beckman Coulter).

*Confocal microscopy analysis*

At the time of collection, cells were washed in PBS, resuspended in DAPI solution (1µg/ml) to counterstain nuclei and transferred on a new glass coverslips in µ-slides (Ibidi, Germany), letting them naturally settle at the bottom. Images were acquired on a confocal laser scanning microscope (LSM510; RRID:SCR_018062, Zeiss).

**Transfection of miRNA inhibitors into LME-sEV**

Transfection of miRCURY LNA™ miRNA Inhibitors against miR-150 (MMU-MIR-150-5P, #339121 YI04101206-ADA, Qiagen), -155 (MMU-MIR-155-5P, #339121 YI04101319-ADA, Qiagen) and -378a (MMU-MIR-378A-5P, #339121 YI04101421-ADA, Qiagen) or scramble control (Negative control A, #339126 YI00199006-ADA, Qiagen) into LME-sEV was performed using HiPerFect® Transfection Reagent (#301704, Qiagen) following a published protocol[58]. Briefly, 20 pmol of each miRCURY LNA™ miRNA Inhibitors were diluted in medium without serum, 2uL transfection reagent were added and mixed by vortexing. The formation of molecular complexes was allowed for 10 min at RT. Next, the complexes were added drop-wise onto LME-sEV and incubated at 37°C for 6h. sEV were washed once in PBS before adding them to CD8$^+$ T-cells for 48h.

### *In vivo* injection of sEV

_Small EV in vivo uptake_

In order to define the uptake of sEV *in vivo*, 100µl of MB570$^+$ LME-sEV (1mg/ml) were injected i.v. in 8 week-old C57BL/6 mice which were euthanized 24h later. Total splenocytes were stained for different cell surface markers (CD4, CD8 and CD19) and analyzed using NovoCyte Quanteon Flow Cytometer (Agilent).

_In vivo treatment with sEV_

Serial injections of LME-sEV during rescue experiment were performed as shown in **Fig.6I**. Briefly, 100µl of LME-sEV (1mg/ml) were injected i.v. the day before the experiment (d-1), together with the cells (d0), and then again at day 3, 5 and 35.

### Culture conditions and *in vitro* sEV treatment

Spleens were collected from C57BL/6 or Foxp3$^{YFP/Cre}$ mice (for Treg isolation) and rapidly transferred in a tube containing PBS (without Ca$^{2+}$/Mg$^{2+}$). Splenocytes isolation was performed by mechanical spleen dissociation through a 100µM strainer (BD Biosciences) and cells were recovered by centrifugation (400g, 4°C, 10 min). Cell pellet was resuspended in ACK lysing solution (Lonza) to lyse red blood cells. Finally, splenocytes were washed in MACS buffer (Miltenyi Biotec), filtered through a 50µM strainer (Celltrics, Sysmex) and counted. CD3$^+$ T-cells were isolated by negative selection using the MojoSort™ Mouse CD3 T-Cell Isolation Kit (Biolegend, San Diego, CA, USA) following the manufacturer's instructions. The isolated T-cell population contained at least 95% of CD3$^+$ T-cells. CD8$^+$ T-cells were isolated by negative selection using the MojoSort™ Mouse CD8 T-Cell Isolation Kit (Biolegend, San Diego, CA, USA) following the manufacturer's instructions. The isolated T-cell population contained at least 95% of CD8$^+$ T-cells. CD8$^+$ T-cells were cultured in anti-CD3 coated wells (10µg/ml; #100302, RRID:AB_312667, Biolegend) in RPMI1640 medium supplemented with 10% Fetal Bovine Serum (FBS), 1% Penicillin/Streptomycin (P/S), IL-2 (10ng/ml; #589104), CD28 (3µg/ml; #102102, RRID:AB_312867, Biolegend) and β-Mercaptoethanol (50µM). Depending on experiment duration, cells were fed with fresh medium every 48h. For intracellular cytokine production, cultured CD8$^+$ T-cells were stimulated overnight with PMA/ionomycin (100nM/1µM) and incubated for a maximum of 4h with Brefeldin A (BFA, 1X). CD4$^+$ T-cells were isolated by negative selection using the MojoSort™ Mouse CD4 T-Cell Isolation Kit (Biolegend, San Diego, CA, USA) following the manufacturer's instructions. The isolated T-cell population contained at least 95% of CD4$^+$ T-cells (comprising CD4$^+$ $T_{conv}$ cells and Treg). CD4$^+$ T-cells were cultured in anti-CD3 coated wells (10µg/ml) with RPMI1640 medium supplemented with 10% FBS, 1% P/S, IL-2 (10ng/ml), and β-Mercaptoethanol (50µM). For immune checkpoint blockade, CD8$^+$ T-cells were treated for 48h using ME-sEV previously coated with 5µg/ml of antibodies directed against PD-L1 (#124302, RRID:AB_961228, Biolegend), MHC-II (#107601, RRID:AB_313316, Biolegend), GAL9 (#136115, RRID:AB_2860679, Biolegend) and VISTA (#BE0310, RRID:AB_2736990, Bioxcell) for 6h at 4°C.

Depending on experiment duration, cells were fed with fresh medium every 48h. B/CLL cells were isolated by negative selection using the MojoSort™ Mouse Pan B-Cell Isolation Kit II (Biolegend, San Diego, CA, USA) following the manufacturer's instructions. The isolated B and CLL cell populations contained at least 90% of CD19$^+$ or CD19$^+$CD5$^+$ double positive cells respectively.

Human PBMC were isolated by density-gradient centrifugation over Linfosep (Biomedics, Madrid, Spain). B-cells were purified with a $CD19^+$ magnetic-bead system (MidiMACS, Miltenyi Biotech, Bergish Gladbash, Germany) according to the manufacturers' instructions. Mean B-cell purity was >99% and the mean percentage of $CD5^+$/$CD19^+$ cells after purification was >98%, as measured by flow cytometry.

Cells used for microarray analysis were cultured for 24h with RPMI1640 medium supplemented with 10% Fetal Bovine Serum (FBS), 1% Penicillin/Streptomycin (P/S), IL-2 (10ng/ml) with either LME-sEV or HCME-sEV.

Cells were incubated with LME-sEV or HCME-sEV based on the physiological amount found in the respective spleen microenvironment (**Fig.1J**). Depending on experiment duration, additional sEV were added every 48h. TCL1-RAB27DKO cells were cultured for 24h with RPMI1640 medium supplemented with 10% Fetal Bovine Serum (FBS), 1% Penicillin/Streptomycin (P/S) with either LME-$sEV_{TCL1}$ or LME-$sEV_{TCL1\text{-}RAB27DKO}$ based on the physiological amount found in the respective spleen microenvironment (**Fig.6F**).

## Flow cytometry sorting of cells

Cells used for microarray analysis were sorted directly from $Foxp3^{YFP/Cre}$ derived purified splenocytes using BD FACSAria™ III Cell Sorter (RRID:SCR_018934). $CD4^+Foxp3^+$ were isolated based on YFP expression, antibodies for $CD8^+$ and $CD4^+Foxp3^-$ staining can be found in **TableS4**.

For experiment requiring to separate $CD4^+Foxp3^+$ from $CD4^+$ $T_{conv}$, cells were sorted directly from LME-sEV treated $Foxp3^{YFP/Cre}$ derived purified splenocytes using BD FACSAria™ III Cell Sorter (RRID:SCR_018934). Treg were isolated based on YFP expression, antibodies for $CD8^+$, $CD4^+$ and $CD19^+$ staining can be found in **TableS4**.

## Flow cytometry analysis of cells

*Surface staining*

Cell surface staining was performed in 100µl of MACS buffer (Miltenyi Biotec) for 30 min on ice in the dark prior analysis on NovoCyte Quanteon Flow Cytometer (Agilent).

Peripheral blood was directly stained for 30 min on ice in the dark, then red blood cells were lysed using RBC Lysis/Fixation Solution (BioLegend), according to the manufacturer's instructions. After washing twice, samples were ready for acquisition on a CytoFLEX analyzer (Beckman Coulter).

*Intracellular staining*

Previously surface stained cells were permeabilized using the eBioscience™ Foxp3/Transcription Factor Staining Buffer Set (ThermoFisher Scientific) following the manufacturer's instructions before intracellular staining. The list of antibodies used for cell surface and intracellular staining can be found in **TableS4**.

## Flow Cytometry Clustering

Clustering analysis of live lymphocytes was performed with Cytosplore software. Briefly, 50,000 events per sample were subjected to Hierarchical Stochastic Neighbor Embedding (HSNE) to generate clusters based on intracellular and transmembrane markers expression. Clusters were generated using the Gaussian mean shift algorithm using the density estimate as input.

## T-cell-mediated cytotoxicity assay

Definition of cytotoxicity of ME-sEV treated-T-cells on CLL cells was performed as previously published[59]. Briefly, C57BL/6 $CD3^+$ T-cells were cultured in 48-well plate on anti-CD3 coated wells (1µg/ml) with RPMI1640 medium supplemented with 10% FBS, 1% P/S and 1µg/ml anti-CD28 antibody for 48h at 37°C, in presence of LME-sEV or HCME-sEV. Treatment with ME-sEV was repeated every 24h. CLL cells ($CD5^+CD19^+$) isolated from TCL1 mouse model were stained with CellTrace CFSE (200 nM, Thermo Fisher). On the day of the assay, CLL target cells were pulsed with 2µg/ml of super antigen (sAg; SEA and SEB; Sigma-Aldrich) for 30 min at 37°C. Target primary CLL cells ($2.5x10^4$) loaded with sAg were added to the ME-sEV pre-treated $CD3^+$ T-cells at a 1:20 (target:effector). Cell mixtures were centrifuged, and the cell pellet incubated for 4 h at 37°C. Cells were stained with TO-PRO-3 viability dye (Thermo Fisher) according to the manufacturer's instructions and T-cell-mediated cytotoxicity against CLL target cells was determined by flow cytometry. Cytotoxicity was calculated as: % target cell death = (% $CFSE^+$ TO-PRO-$3^+$ target cells incubated with effector T-cells - % of $CFSE^+$ TO-PRO-$3^+$ target cells incubated alone) × 100/(100 - % of $CFSE^+$ TO-PRO-$3^+$ target cells incubated alone).

**T-cell:CLL (tumor) cell conjugation and immunological synapse assays**

Immune synapse assays and quantitative analysis were performed as previously described[59]. Briefly, purified murine $CD3^+$ T-cells and purified $CD5^+CD19^+$ CLL cells from TCL1 mouse were incubated for 48h at 37°C or in the presence of LME-sEV or HCME-sEV. Treatment with ME-sEV was repeated every 24h. Next, the same CLL cells were stained with CellTracker Blue CMAC according to the manufacturer's instructions and pulsed with 2µg/ml of super antigen (sAg; SEA and SEB; Sigma-Aldrich) for 30 min at 37°C before washing. Tumor cells were then pooled with an equal number of T-cells ($1×10^6$; to ensure identical cell numbers per sample and allow accurate evaluation of changes in % of conjugated T-cells and F-actin immune synapse formation with treatment), centrifuged at 260g (5 min) and incubated at 37°C for 10 min ($CD8^+$ T-cells). Cells were then transferred onto microscope slides (Polysine slides; Thermo Scientific) using a cell concentrator (Cytofuge 2) and fixed for 15 min at room temperature with 3% formaldehyde (Thermo Scientific) in PBS.

Immunofluorescence (IF) labeling was done using Cytofuge2 cell concentrator units. After fixing, cells were permeabilized with 0.3% Triton X-100 (Sigma-Aldrich) in PBS for 5 min and treated for 10 min with 5% goat serum (Sigma-Aldrich) in PBS blocking solution. Primary and secondary antibodies (Alexa Fluor 488 or 647, Thermo Fisher Scientific) were applied sequentially for 45 min at 4°C in 5% goat serum (Sigma-Aldrich) in PBS blocking solution. F-actin was stained with rhodamine phalloidin (Thermo Fisher) following the manufacturer's instructions and applied alone or with the secondary antibody. After washing, the cell specimens were sealed with coverslips using mounting solution FluorSaveTM reagent (Merck Millipore). The specificity of staining was optimized and controlled by using appropriate dilutions of isotype-control, primary Abs and subsequent fluorescent secondary Abs. Background staining using Abs alone was compared with positively stained cells and was not visible when using identical acquisition settings. Medial optical section (or Z-stacks for 3D volume images) images were captured with a high-sensitivity A1R confocal microscope (with gallium arsenide phosphide, GaAsP detector) using a 63X/1.40 oil objective with NIS-elements imaging software (Nikon). Detectors were set to detect an optimal signal below saturation limits. Fluorescence was acquired sequentially to prevent passage of fluorescence from other channels (DU4 sequential acquisition). Image sets to be compared were acquired during the same session using identical acquisition settings.

**Real-time PCR**

*RNA isolation*

Cellular and sEV RNA were isolated using NucleoZOL, one phase RNA purification reagent and columns from the NucleoSpin RNA Set for NucleoZOL Mini kit, according to manufacturer's instructions (Macherey-Nagel). For transcriptomics analysis using microarrays or RNA sequencing, RNA was quantified with Qubit (Thermo Scientific) and the quality was assessed with the Fragment Analyzer 5200 using RNA kits (Agilent). For purified human CLL cells, total RNA was extracted in a single step using TriPure Isolation Reagent (Roche Applied Science, Vilvoorde, Belgium).

### *MicroRNA detection in sEV and in sEV-treated $CD8^+$ T-cells*

MicroRNA were quantified by RT-qPCR performed using TaqMan™ MicroRNA assays, TaqMan™ MicroRNA Reverse Transcription Kit, (Thermo Scientific), and the Takyon™ Low ROX Probe 2X MasterMix dTTP blue (Eurogentec) [15,20]. The following probes were used: miR-21 (#002438), miR-146a (#000468), miR-378a (#000567), miR-210 (#000512), miR-27a (#000408), miR-150 (#000473), miR-155 (#002623) and U6 (#001973).

### *Gene expression in cells*

Reverse transcription of mRNA was performed in a SimpliAmp™ Thermal Cycler (ThermoFisher) using FastGene® Scriptase II cDNA 5x ReadyMix (Nippon genetics). Real-time PCR was performed in the QuantStudio™ 5 Real-Time PCR System (ThermoFisher) using the SYBR Green detection system. The primers were for *Gzmb* F: 5’-CAGGAGAAGACCCAGCAAGTCA-3’ and R: 5’-CTCACAGCTCTAGTCCTCTTGG-3’, *Prf1* F: 5’-TGGTGGGACTTCAGCTTTCC-3’ and R: 5’-TGCTTGCATTCTGACCGAGT-3’, *Slc7a5* F: 5’-CATCAACGACTCTGTTGTAGACC-3’ and R: 5’-CGCTGGATACAGGATTGCGG-3’, *Itpkc* F: 5’-CATCACCCCAGAGACTCCTGA-3’ and R: 5’-TTCTTCCAGGGCTTGCTTCCAG-3’ and *Fgr* F: 5’-GAGGCGGGTAGCACCTCAC-3’ and R: 5’-CCCATTCCAGATGCCCCCAC-3’ were from Eurogentec. For RNA isolated from purified human CLL cells, cDNA was generated by a retrostranscription using the qScript™ cDNA Synthesis Kits (Quanta Biosciences/VWR International, Leuven, Belgium). Real-time PCR was performed in the QuantStudio™ 5 Real-Time PCR System (ThermoFisher) using the SYBR Green detection system. The primers used were *28S* F: 5’-GGGTGGTAAACTCCATCTAAGG-3’ and R: 5’-GCCCTCTTGAACTCTCTCTTC-3’, *RAB27a* F: 5’-TGGGAGACTCTGGTGTAGGG-3’ and R: 5’-ACTGGCTCTGTACACCACTC-3’, *RAB10* F: 5’-TCCCAATGGCGAAGAAGAC-3’ and R: 5’-TGATCTTGAAGTCTATTCCTATGGT-3’, *RAB35* F: 5’-GCACCATCACCTCCACGTAT-3’ and R: 5’-CCGCTTGACGTTGACAAAGG-3’, *RAB40c* F: 5’-CGTACGCCTACAGTAACGGGAT-3’ and R: 5’-GTAGGACCTGAAGATGGTGCAG-3’, *RAB31* F: 5’-TGTGCCTTCTCGGGGACAC-3’ and R: 5’-GCCCCAATAGTAGGGCTGAT-3’, *PDCD6IP* F: 5’-TCGAGACGCTCCTGAGATATT-3’ and R: 5’-AGCCAGTTTTACAGAGCCTCC-3’, *RAB7A* F: 5’-ATGCACTTAAGCAGGAAACGG-3’ and R: 5’-TGGCCCGGTCATTCTTGTC-3’.

## Transcriptomics

### *RNA-sequencing*

Librairies were prepared with the QuantSeq 3' mRNA-Seq Library Prep Kit FWD for Illumina (Lexogen), according to manufacturer’s instructions, with the addition of UMI. Barcoded samples were pooled, diluted, loaded onto a NextSeq 500/500 Mid Output flowcell (130M reads, Illumina) and single-end sequencing was performed on a NextSeq 550 (Illumina). After initial QCs using FastQC (https://www.bioinformatics.babraham.ac.uk/projects/fastqc/; RRID:SCR_014583) and FastQ Screen (https://www.bioinformatics.babraham.ac.uk/projects/fastq_screen/; RRID:SCR_000141), fastq files were processed using a local Snakemake workflow including the following main steps. First, raw reads were trimmed from their UMI index, poly A and adapter sequences using a combination of dedicated scripts and cutadapt (v2.10). Next, filtered reads were submitted for mapping (STAR v2.5.3a; RRID:SCR_004463) on the Mouse Reference genome (GRCm38). Collapsing of reads originating from the same fragment was achieved with umi_tools (v1.0.0) and counting was perfomed with featureCounts (subread v2.0.0; RRID:SCR_012919).

### *Gene expression analysis*

Differential expression analysis was performed using the *limma*-based R/Bioconductor EdgeR package (RRID:SCR_012802)[60] for *in vitro* treated samples or using the nonparametric NOISeq (RRID:SCR_003002) package[61] for *in vivo* treated samples presenting lower sequencing depth and more intrinsic variability. Genes with less than 5 counts were filtered out and counts were processed for trimmed mean of M values (TMM) normalization. Differential expression of genes across samples (DEG) was assessed by imposing a FDR < 0.05 and a $\log_2$ fold change cut-off of 1. The *pheatmap* function was used for data visualization. For k-means clustering, the 2,500 most variable genes were included and six clusters were defined according to the elbow method with the iDEP9.2 online tool, followed by Gene Ontology analysis for Biological Process (http://bioinformatics.sdstate.edu/idep/).

*Gene ontology analysis*

Ontology analyses of differentially expressed genes was performed with g:Profiler web server (RRID:SCR_006809) for functional profiling (https://biit.cs.ut.ee/gprofiler/gost).

*sEV score*

We used public datasets to compare gene expression profiles of normal B-cells and CLL cells in Human (GSE67640) and Mouse (GSE175564)[16,21]. GSE67640 was analyzed with GEO2R online tool (RRID:SCR_016569; *limma* (RRID:SCR_010943), Benjamini & Hochberg (False discovery rate) adjusted p-value < 0.05, and log2FC > 1). The DEG lists were compared to a list of 143 genes (combining genes involved in sEV biology based on literature review and Top100 proteins found in sEV according to http://microvesicles.org, listed in TableS2). The expression values of genes present in both lists (shown in the heatmaps) were used to compute sEV-scores for Human and Mouse B and CLL cells, corresponding to a z-scored-geometric mean of expression values.

**Proteomics**

*Sample preparation of sEV proteome*

Starting from the same amount of sEV proteins between conditions, each sEV sample was split into triplicates. Proteins were extracted with Sodium Deoxycholate (SDC, 3% final concentration) following a 30 min incubation at 4°C in presence of protease inhibitors (cOmplete™ EDTA-free Protease Inhibitor Cocktail, Roche). Following centrifugation at 16,000g for 10 min, supernatants were subjected to protein reduction (5mM DTT, 1h incubation at 37°C) and alkylation (10mM IAA, 45 min at room temperature in the dark). Samples were then acidified with formic acid (FA, 1% final concentration), and SDC was precipitated after centrifugation at 16,000 g for 15 min. The supernatants were transferred into clean tubes and supplied with pre-prepared SP3 beads (Fisher Scientific, #09-981-121, #09-981-123). One volume of acetonitrile (ACN, 100% v/v) was added immediately followed by incubation at room temperature for 10 min. The supernatants were removed using a magnetic rack, and the beads were rinsed first with 200µL of 70% ethanol, and then further rinsed with 180µL of 100% ACN. Rinsed beads were reconstituted in 30µL digestion buffer (50mM ammonium bicarbonate, pH 8). Protein digestion was performed with 1µg of sequencing grade trypsin (Promega, V5111) for 4 h at 37°C, then incubated overnight at 37°C with additional 1µg trypsin. After digestion, ACN was added to each sample to a final concentration of 95%. Mixtures were incubated for 10 min at room temperature and then placed on a magnetic rack for 2 min. The supernatants were discarded, and the beads were rinsed with 180µL of 100% ACN. Rinsed beads were reconstituted in 30µL LC-MS grade-water and incubated for 5 min at room temperature to elute the digested peptides. The eluted peptide samples were acidified with formic acid to a final concentration of 0.1%.

*Proteomic sample preparation of sEV-treated cells*

$CD8^+$ T-cells treated with sEV were collected in triplicate after 24h and 4 days of treatment. After being harvested, cells were washed twice with cold PBS. Next, pellets were re-suspended in lysis buffer (6M urea, 2M thiourea, 50 mM ammonium bicarbonate, pH 8) supplemented with fresh prepared cOmplete™ EDTA-free Protease Inhibitor Cocktail (Roche). After incubation at 22°C for 30 min, samples were sonicated (3 sec sonication and 2 sec pause for a total of 30 sec). The supernatants were taken into new tubes following centrifugation at 16,000g for 15 min. Protein quantification assay of the cell extracts was performed with Bradford assay (Sigma Aldrich, B6916) to estimate the concentrations. A total of 30µg of each sample were taken for protein reduction and alkylation and digested with Lys-C (FUJIFILM Wako, 125-05061) at 1:30 ratio (enzyme/protein substances) for 4h at 37°C, then samples were diluted 4 times with 50mM ammonium bicarbonate and digested overnight with 1µg of trypsin at 37 °C. The protein digestion was terminated with the addition of formic acid (1% final concentration). The digested peptides were cleaned up with reverse phase Sep-Pak C18 1 cc Vac Cartridge (Waters, WAT054955) and eluted with 1ml 50% ACN. Eluted peptides were dried by Speedvac (Thermo Fisher Scientific) and re-suspended in 0.1% formic acid. Nanodrop was used to estimate the peptide concentration.

*LC-MS/MS data acquisition*

Digested peptides were measured by LC-MS/MS on either Q-Exactive Plus or Q-Exactive HF mass spectrometer (Thermo Fisher) connected to a Dionex Ultimate 3000 (Thermo Fisher). A total of 400ng of peptides were loaded onto a trap column (Acclaim PepMap 75µm x 2cm, C18, 3µm) and separated on a 25cm Acclaim pepmap RSLC column (75µm x 25cm, C18, 2µm) using an 150 min gradient with a flow rate of 0.3µL/min. MS data were acquired in data dependent mode (DDA). Survey scans of peptide precursors from 375 to 1500m/z were performed at 70,000 resolution with a $3\times10^6$ ion count target and the top 12 abundant peaks from survey scan were selected for fragmentation. Tandem MS was performed by isolation at 1.4m/z with the quadrupole, HCD fragmentation with a normalized collision energy of 28. The MS2 ion count target was set to $1\times10^5$ and the max injection time was 45ms. Only precursors with a charge state of 2–7 were sampled for MS2. The dynamic exclusion duration was set to 20s with a 10ppm tolerance around the selected precursor and its isotopes.

*Database searching and protein identification*

All raw data was analyzed with MaxQuant (version 1.6.7.0; RRID:SCR_014485) and searched with Andromeda against mus musculus database from Uniprot. The minimal peptide length was set to 7 amino acids and the maximum of 3 missed cleavages were allowed. The search included variable modifications of methionine oxidation and N-terminal acetylation, deamidation (N and Q) and fixed modification of carbamidomethyl cysteine. The "Match between run" was checked within 1 min retention time window. Mass tolerance for peptide precursor and fragments were set as 10 ppm and 20 ppm, respectively. The FDR was set to 0.01 for peptide and protein identifications. Label-free quantification was used for quantitative data of identified protein based on its razor and unique peptides. Proteus, an R package, was used for downstream analysis of MaxQuant (RRID:SCR_014485) output. The input for Proteus is the evidence file. Evidence data are aggregated into peptides and then into proteins.

*Proteomic data analysis*

For sEV proteome, LFQ intensities of proteins identified in HCME-sEV, LME-sEV, and LME-sEV TCL1-RAB27DKO were processed as follows. We first removed zero intensities across all samples and then we performed log2 transformation and quantile normalization. As samples were acquired in two batches, we performed batch correction using the *combat* algorithm. Values were then imported in the MaxQuant Perseus software (version 1.6.15.0). Two-sample tests were performed and proteins with a q-value < 0.05 (Benjamini-Hochberg FDR) were considered statistically enriched in a condition. Coordinates from Principal Component Analysis (PCA) were exported and plotted with GraphPad Prism (version 9.1.2; RRID:SCR_002798). Heat maps were generated with the R pheatmap function.

*Gene and protein ontology analysis*

Ontology analyses of differentially expressed proteins was performed with g:Profiler (RRID:SCR_006809) web server for functional profiling (https://biit.cs.ut.ee/gprofiler/gost).

## Metabolomics analysis

*Detection of metabolic protein by Western-blot*

To assess alterations of metabolic protein expression induced by ME-sEV treatment, total proteins isolated from treated CD8$^+$ T-cells were subjected to western blot: PFKP (#ab204131, RRID:AB_2828009, Abcam), PHGDH (#HPA021241, RRID:AB_1855299, Sigma Aldrich), PCK2 (#6924S, RRID:AB_10836185, Cell Signaling), MCT4 (#sc-50329, RRID:AB_2189333, Santa Cruz) and GLUT1 (#PA1-46152, RRID:AB_2302087, Thermofisher).

*Stable isotope tracing and metabolite extraction*

Stable isotope tracing experiments with [U-$^{13}$C]-glucose tracer (Cambridge Isotope Laboratories, CLM-1396) were performed in RPMI-1640 medium supplemented with 11.1mM [U-$^{13}$C]-glucose, 2mM glutamine, 10% Fetal Bovine Serum (FBS), 1% Penicillin/Streptomycin (P/S), IL-2 (10ng/ml), CD28 (3µg/ml). For [U-$^{13}$C]-glutamine tracing (Cambridge isotope Laboratories, CLM-1822) RPMI 1640 medium for SILAC (#A24942-01) was used and supplemented as above with the addition of 1.15mM arginine and 0.219mM lysine. A total of 1x10$^6$ cells were seeded in triplicates in 24-well plates pre-coated with anti-CD3 antibody (10µg/ml), already in the [U-$^{13}$C]-glucose or glutamine medium. At time-point of metabolite extraction, cell number and volume were determined to calculate packed cell volume (PCV). For metabolite extraction, cells were collected and pelleted at 350g for 5 min at 4°C and the medium was stored at -80°C to determine metabolites exchange rates. To determine the basal medium composition for the subsequent calculation of exchange rates, identical medium was incubated in empty 24 wells throughout the experiment and analyzed in parallel to the medium samples. The cell pellet was then washed with ice-cold 1xPBS solution. 400µl ice-cold extraction fluid [acetonitrile/H2OMQ/methanol (ratio, 3:2:5); liquid chromatography–MS (LC-MS) grade solvents)] was added to each cell pellet. Cells were mixed for 10 min on a thermomixer at 4°C at maximum speed, then the tubes were centrifuged for 10 min at 16,100g at 4°C. 100µL of the supernatant was collected and transferred to an already-cooled LC-MS glass vial with inserts and stored at -80°C until measurement.

*YSI measurements and medium exchange rates*

Medium samples were filtered (PVDF, 0.22µm) prior measurement to remove particles. Absolute quantitative values for lactic acid, glutamine, glutamic acid and glucose were acquired using a YSI 2950D Biochemistry Analyzer (Kreienbaum KWM). For a precise and reliable quantification, external concentration curves of each target compound were prepared and measured in triplicates. Absolute uptake and release rates were calculated as previously described[62].

*LC-MS Measurements*

The following analytical conditions are based on a previously published protocol[62]. Metabolite analyses were performed using a Thermo Vanquish Flex Quaternary LC coupled to a Thermo Q Exactive HF mass spectrometer. Chromatography was carried out with a SeQuant ZIC-pHILIC 5µm polymer (150 x 2.1mm) column connected to the corresponding SeQuant ZIC-pHILIC Guard (20 x 2.1mm) pre-column. Column temperature was maintained at 45°C. The flow rate was set to 0.2ml/min and the mobile phases consisted of 20mmol/L ammonium carbonate in water, pH 9.2 (Eluent A) and Acetonitrile (Eluent B). The gradient was: 0 min, 80% B; 2 min, 80% B; 17 min, 20% B; 18 min 20% B; 19 min 80 % B; 20 min 80% B (0.4ml/min); 24 min 80% B (0.4ml/min); 24.5 min 80% B. The injection volume was 5µL. All MS experiments were performed using electrospray ionization with polarity switching enabled (+ESI/-ESI). The source parameters were applied as follows: sheath gas flow rate, 25; aux gas flow rate, 15; sweep gas flow rate, 0; spray voltage, 4.5 kV (+) / 3.5 kV (–); capillary temperature, 325°C; S-lense RF level, 50; aux gas heater temperature, 50°C. The Orbitrap mass analyzer was operated at a resolving power of 30,000 in full-scan mode (scan range: m/z 75…1000; automatic gain control target: 1e6; maximum injection time: 250 ms). Data were acquired with Thermo Xcalibur software (Version 4.3.73.11; RRID:SCR_014593) and analyzed with TraceFinder (Version 4.1). Subsequent data analysis for normalization and natural isotope subtraction were performed using in house scripts as previously described[62].

*Oxygen consumption rate using seahorse*

A Seahorse XFe96 Bioanalyser (RRID:SCR_019545, Agilent) was used to determine basal oxygen consumption rate (OCR) of CD8$^+$ T cells after *ex vivo* treatment with ME-sEV (96h), following manufacturer's instructions using WAVE software (RRID:SCR_014526). Treated cells were washed in assay media (XF Base media (Agilent) with glucose (10mM), sodium pyruvate (1mM) and L-glutamine (2mM; Gibco), pH 7.4 at 37 °C) before being plated onto Seahorse cell culture plates coated with Cell-Tak (Corning) at $3.5 \times 10^5$ cells/well followed by a gentle centrifugation (5min, 300g, RT, 0 break).

**Statistical analysis of sEV gene expression in CLL patient cohort**

*Differential expression analysis and predictive power*

CT values obtained from Real-time PCR were normalized using CTs of ribosomal RNA 28S as a housekeeping gene. Differential expression analysis was perform to check which genes was associated to patient groups by "limma" package of R/Bioconductor (RRID:SCR_010943)[63].

*Survival analysis and risk score*

Univariate Cox regression models independently for TFSOS were built. R-package "survival" was used for the analysis and visualization of the data. Normalized log-expression of the considered genes were used for the regression model. Individual genes were combined to a risk score with a better prognostic properties based on previous publications[64,65]. However, in the current study we weighted contribution of each gene by its p-value: the risk score (RS) for *i*-th patient was calculated as

$$RS_i = -\sum_j \log(P_j) \cdot H_j \cdot X_{i,j}$$

where $P_j$ and $H_j$ – a p-value of likelihood ratio test and a log hazard ratio from a univariate Cox model of the *j*-th gene accordingly, $X_{i,j}$ is the log-expression of the *j*-th gene in *i*-th patient. Here we run an exhaustive search of all gene combinations and selected the Cox model with the minimal p-value. Kaplan-Meier plots were built to visualize linkage between genes or risk score and patient survival. Median level was used to dichotomize patients into two groups. Significance of the variation in risk score regarding mutational status and prognosis markers for each patient was assessed by ANOVA.

*Analysis using logistic regression*

We tried to link gene expression and binary outcomes using logistic regression (`glm` from R/Bioconductor). In order to avoid uncertainty resulting from gene-gene correlation, we used a similar approach as for Cox regression. First, coefficients or log-odds ratios and p-values were determined from univariable logistic models for each gene independently and then combined into a score using the same formula as for the risk score in Cox regression, with log-odds ratios instead of log-hazard ratios.

**Statistical analysis**

Statistical analysis was performed using GraphPad Prism software (version 9.1.2; RRID:SCR_002798). Data are presented as mean ± standard error of mean (SEM). The log-rank test was used for the survival curves. For the percentage of CLL cells in mice over time, we performed two-way ANOVA followed by Bonferroni's multiple comparison test. The unpaired t test was used for the rest of the figures. A *p*-value lower than 0.05 was considered statistically significant. Significance displayed in each figure is explained in figure legends.

**Data Availability Statement:** The datasets presented in this study are openly available in the Gene Expression Omnibus with the accession numbers GSE188898, GSE189391, GSE190789, GSE190790, and GSE191186.

**Acknowledgments:** We thank Pr. Carlo Croce and Pr. John Byrd (Ohio State University, US) for the kind gift of Eμ-*TCL1* mouse, and Pr. Miguel Seabra and Dr Tanya Tolmachova (Imperial College London, UK) for the RAB27DKO mouse. We thank Dr Javier Alves Ferreira (JAF, Laboratoire National de Santé, Luxembourg) for the histopathology expertise. We thank the National Cytometry Platform (LIH; Dr Antonio Cosma, Dr Céline Hoffmann, Thomas Cerutti, Fanny Hedin, Maria Konstantinou) for assistance in flow cytometry, imaging flow cytometry, confocal microscopy and FACS experiments, the LUXGEN platform (LIH/LNS; Nathalie Nicot, Elise Mommaerts, Arnaud Muller and Dr Daniel Stieber) for RNA sequencing, the bioinformatics platform (LIH; Tony Kaoma and Kim Sang Yoon) for assistance, and the Animal Facility (LIH) staff. We thank the Metabolomics Platform (University of Luxembourg, Christian Jäger) for GC-MS measurements and Xiangyi Dong and Floriane Vanhalle for providing technical and analytical support. Furthermore, we thank the Metabolomics core facility (LIH, Antoine Lesur and François Bernardin) for technical and analytical support. Special thanks to Dr Martina Seiffert (DKFZ, Germany) for the useful scientific discussions and for providing the Eμ-*TCL1* animals. Finally, we thank Dr Marina Wierz, Bilgee Bayanaa and Sandrine Pierson (LIH) for technical support.

**Funding:** This work was supported by grants from the Luxembourg National Research Fund (FNR) to EG, EM and JP (PRIDE15/10675146/CANBIO, INTER/DFG/16/11509946, C20/BM/14582635, and C20/BM/14592342), to JM (ATTRACT grant A18/BM/11809970), and to MM (PEARL grant P16/BM/11192868), from FNRS-Télévie to EV, PEM, AL, and SG (7.4509.20, 7.8506.19, 7.4503.19, and 7.6604.21), from the European commission to PEM (H2020-MSCA-IF-2020: 101029602).

**Authorship Contributions:** EG designed and performed experiments, analyzed results and wrote the manuscript. EV, PEM and AL helped in performing experiments, analyzing data and writing the manuscript. SG provided assistance with mice. FX and GD provided expertise on proteomics and performed the analyses. NI and AGR performed CD8$^+$ T-cell cytotoxic assays and immune synapse analyses. FKB and MM performed electron microscopy pictures of sEV. MB and JM provided expertise on metabolomics and performed the analyses. BS provided cDNA from cohort of CLL patients, patients' data and provided expertise for analyses. EM and JP designed and supervised the study, performed bioinformatics analyses, analyzed results, and wrote the final version of the manuscript. All authors revised the manuscript.

**Note:** Supplementary data for this article are available at Blood Cancer Discovery Online (https://bloodcancerdiscov.aacrjournals.org/).

## References

1.Beach A, Zhang HG, Ratajczak MZ, Kakar SS. Exosomes: an overview of biogenesis, composition and role in ovarian cancer. *J Ovarian Res*. 2014;7:14.
2.Raposo G, Stoorvogel W. Extracellular vesicles: exosomes, microvesicles, and friends. *J Cell Biol*. 2013;200(4):373-383.
3.Colombo M, Moita C, van Niel G, et al. Analysis of ESCRT functions in exosome biogenesis, composition and secretion highlights the heterogeneity of extracellular vesicles. *J Cell Sci*. 2013;126(Pt 24):5553-5565.

4.Kumar B, Garcia M, Weng L, et al. Acute myeloid leukemia transforms the bone marrow niche into a leukemia-permissive microenvironment through exosome secretion. *Leukemia*. 2018;32(3):575-587.

5.Prieto D, Sotelo N, Seija N, et al. S100-A9 protein in exosomes from chronic lymphocytic leukemia cells promotes NF-kappaB activity during disease progression. *Blood*. 2017;130(6):777-788.

6.Mannavola F, Tucci M, Felici C, Passarelli A, D'Oronzo S, Silvestris F. Tumor-derived exosomes promote the in vitro osteotropism of melanoma cells by activating the SDF-1/CXCR4/CXCR7 axis. *J Transl Med*. 2019;17(1):230.

7.Gargiulo E, Paggetti J, Moussay E. Hematological Malignancy-Derived Small Extracellular Vesicles and Tumor Microenvironment: The Art of Turning Foes into Friends. *Cells*. 2019;8(5).

8.Tsukada N, Burger JA, Zvaifler NJ, Kipps TJ. Distinctive features of "nurselike" cells that differentiate in the context of chronic lymphocytic leukemia. *Blood*. 2002;99(3):1030-1037.

9.Burger JA, Ghia P, Rosenwald A, Caligaris-Cappio F. The microenvironment in mature B-cell malignancies: a target for new treatment strategies. *Blood*. 2009;114(16):3367-3375.

10.Wierz M, Pierson S, Guyonnet L, et al. Dual PD1/LAG3 immune checkpoint blockade limits tumor development in a murine model of chronic lymphocytic leukemia. *Blood*. 2018;131(14):1617-1621.

11.Radulovic K, Rossini V, Manta C, Holzmann K, Kestler HA, Niess JH. The early activation marker CD69 regulates the expression of chemokines and CD4 T cell accumulation in intestine. *PLoS One*. 2013;8(6):e65413.

12.Shiow LR, Rosen DB, Brdickova N, et al. CD69 acts downstream of interferon-alpha/beta to inhibit S1P1 and lymphocyte egress from lymphoid organs. *Nature*. 2006;440(7083):540-544.

13.Smallwood DT, Apollonio B, Willimott S, et al. Extracellular vesicles released by CD40/IL-4-stimulated CLL cells confer altered functional properties to CD4+ T cells. *Blood*. 2016;128(4):542-552.

14.Paggetti J, Haderk F, Seiffert M, et al. Exosomes released by chronic lymphocytic leukemia cells induce the transition of stromal cells into cancer-associated fibroblasts. *Blood*. 2015;126(9):1106-1117.

15.Haderk F, Schulz R, Iskar M, et al. Tumor-derived exosomes modulate PD-L1 expression in monocytes. *Sci Immunol*. 2017;2(13).

16.Filarsky K, Garding A, Becker N, et al. Kruppel-like factor 4 (KLF4) inactivation in chronic lymphocytic leukemia correlates with promoter DNA-methylation and can be reversed by inhibition of NOTCH signaling. *Haematologica*. 2016;101(6):e249-253.

17.Hsu C, Morohashi Y, Yoshimura S, et al. Regulation of exosome secretion by Rab35 and its GTPase-activating proteins TBC1D10A-C. *J Cell Biol*. 2010;189(2):223-232.

18.Stenmark H. Rab GTPases as coordinators of vesicle traffic. *Nat Rev Mol Cell Biol*. 2009;10(8):513-525.

19.Matsui T, Osaki F, Hiragi S, Sakamaki Y, Fukuda M. ALIX and ceramide differentially control polarized small extracellular vesicle release from epithelial cells. *EMBO Rep*. 2021;22(5):e51475.

20.Paggetti J, Berchem G, Moussay E. Stromal cell-induced miRNA alteration in chronic lymphocytic leukemia: how a minute and unavoidable cell contamination impairs miRNA profiling. *Leukemia*. 2013;27(8):1773-1776.

21.Gonder S, Largeot A, Gargiulo E, et al. The Tumor Microenvironment-Dependent Transcription Factors AHR and HIF-1α Are Dispensable for Leukemogenesis in the Eμ-TCL1 Mouse Model of Chronic Lymphocytic Leukemia. *Cancers*. 2021;13(18):4518.

22.Schiller LT, Lemus-Diaz N, Rinaldi Ferreira R, Boker KO, Gruber J. Enhanced Production of Exosome-Associated AAV by Overexpression of the Tetraspanin CD9. *Mol Ther Methods Clin Dev*. 2018;9:278-287.

23.Wei D, Zhan W, Gao Y, et al. RAB31 marks and controls an ESCRT-independent exosome pathway. *Cell Res*. 2021;31(2):157-177.

24.Kalluri R, LeBleu VS. The biology, function, and biomedical applications of exosomes. *Science*. 2020;367(6478).

25.Moussay E, Wang K, Cho JH, et al. MicroRNA as biomarkers and regulators in B-cell chronic lymphocytic leukemia. *Proc Natl Acad Sci U S A*. 2011;108(16):6573-6578.

26.Andreola G, Rivoltini L, Castelli C, et al. Induction of lymphocyte apoptosis by tumor cell secretion of FasL-bearing microvesicles. *J Exp Med*. 2002;195(10):1303-1316.

27.Chen Z, You L, Wang L, et al. Dual effect of DLBCL-derived EXOs in lymphoma to improve DC vaccine efficacy in vitro while favor tumorgenesis in vivo. *J Exp Clin Cancer Res*. 2018;37(1):190.

28.Mak TW, Grusdat M, Duncan GS, et al. Glutathione Primes T Cell Metabolism for Inflammation. *Immunity*. 2017;46(6):1089-1090.

29.Schurich A, Pallett LJ, Jajbhay D, et al. Distinct Metabolic Requirements of Exhausted and Functional Virus-Specific CD8 T Cells in the Same Host. *Cell Rep*. 2016;16(5):1243-1252.

30.Zheng L, Qin S, Si W, et al. Pan-cancer single-cell landscape of tumor-infiltrating T cells. *Science*. 2021;374(6574):abe6474.

31.Zhang F, Li R, Yang Y, et al. Specific Decrease in B-Cell-Derived Extracellular Vesicles Enhances Post-Chemotherapeutic CD8(+) T Cell Responses. *Immunity*. 2019;50(3):738-750 e737.

32.Kim TD, Lee SU, Yun S, et al. Human microRNA-27a* targets Prf1 and GzmB expression to regulate NK-cell cytotoxicity. *Blood*. 2011;118(20):5476-5486.

33.Wang P, Gu Y, Zhang Q, et al. Identification of Resting and Type I IFN-Activated Human NK Cell miRNomes Reveals MicroRNA-378 and MicroRNA-30e as Negative Regulators of NK Cell Cytotoxicity. *The Journal of Immunology*. 2012;189(1):211.

34.Trotta R, Chen L, Costinean S, et al. Overexpression of miR-155 causes expansion, arrest in terminal differentiation and functional activation of mouse natural killer cells. *Blood*. 2013;121(16):3126-3134.

35.Kim N, Kim M, Yun S, et al. MicroRNA-150 regulates the cytotoxicity of natural killers by targeting perforin-1. *J Allergy Clin Immunol*. 2014;134(1):195-203.

36.Bobrie A, Krumeich S, Reyal F, et al. Rab27a supports exosome-dependent and -independent mechanisms that modify the tumor microenvironment and can promote tumor progression. *Cancer Res*. 2012;72(19):4920-4930.

37.Jae N, McEwan DG, Manavski Y, Boon RA, Dimmeler S. Rab7a and Rab27b control secretion of endothelial microRNA through extracellular vesicles. *FEBS Lett*. 2015;589(20 Pt B):3182-3188.

38.Ostrowski M, Carmo NB, Krumeich S, et al. Rab27a and Rab27b control different steps of the exosome secretion pathway. *Nat Cell Biol*. 2010;12(1):19-30; sup pp 11-13.

39.Xing C, Li H, Li RJ, et al. The roles of exosomal immune checkpoint proteins in tumors. *Mil Med Res*. 2021;8(1):56.

40.Moussay E, Palissot V, Vallar L, et al. Determination of genes and microRNAs involved in the resistance to fludarabine in vivo in chronic lymphocytic leukemia. *Mol Cancer*. 2010;9:115.

41.Yeh YY, Ozer HG, Lehman AM, et al. Characterization of CLL exosomes reveals a distinct microRNA signature and enhanced secretion by activation of BCR signaling. *Blood*. 2015;125(21):3297-3305.

42.Szajnik M, Czystowska M, Szczepanski MJ, Mandapathil M, Whiteside TL. Tumor-derived microvesicles induce, expand and up-regulate biological activities of human regulatory T cells (Treg). *PLoS One*. 2010;5(7):e11469.

43.Clayton A, Al-Taei S, Webber J, Mason MD, Tabi Z. Cancer exosomes express CD39 and CD73, which suppress T cells through adenosine production. *J Immunol*. 2011;187(2):676-683.

44.Morrissey SM, Zhang F, Ding C, et al. Tumor-derived exosomes drive immunosuppressive macrophages in a pre-metastatic niche through glycolytic dominant metabolic reprogramming. *Cell Metab*. 2021;33(10):2040-2058 e2010.

45.Li C, Phoon YP, Karlinsey K, et al. A high OXPHOS CD8 T cell subset is predictive of immunotherapy resistance in melanoma patients. *J Exp Med*. 2022;219(1).

46.Sadik A, Somarribas Patterson LF, Ozturk S, et al. IL4I1 Is a Metabolic Immune Checkpoint that Activates the AHR and Promotes Tumor Progression. *Cell*. 2020;182(5):1252-1270 e1234.

47.Tolmachova T, Abrink M, Futter CE, Authi KS, Seabra MC. Rab27b regulates number and secretion of platelet dense granules. *Proc Natl Acad Sci U S A*. 2007;104(14):5872-5877.

48.Stinchcombe JC, Barral DC, Mules EH, et al. Rab27a is required for regulated secretion in cytotoxic T lymphocytes. *J Cell Biol*. 2001;152(4):825-834.

49.Okoye IS, Coomes SM, Pelly VS, et al. MicroRNA-Containing T-Regulatory-Cell-Derived Exosomes Suppress Pathogenic T Helper 1 Cells. *Immunity*. 2014;41(3):503.

50.Wang JS, Wang FB, Zhang QG, Shen ZZ, Shao ZM. Enhanced expression of Rab27A gene by breast cancer cells promoting invasiveness and the metastasis potential by secretion of insulin-like growth factor-II. *Mol Cancer Res*. 2008;6(3):372-382.

51.Ding W, LaPlant BR, Call TG, et al. Pembrolizumab in patients with CLL and Richter transformation or with relapsed CLL. *Blood*. 2017;129(26):3419-3427.

52.Gargiulo E, Morande PE, Largeot A, Moussay E, Paggetti J. Diagnostic and Therapeutic Potential of Extracellular Vesicles in B-Cell Malignancies. *Front Oncol*. 2020;10:580874.

53.Stamatopoulos B, Van Damme M, Crompot E, et al. Opposite Prognostic Significance of Cellular and Serum Circulating MicroRNA-150 in Patients with Chronic Lymphocytic Leukemia. *Mol Med*. 2015;21:123-133.

54.Stamatopoulos B, Smith T, Crompot E, et al. The Light Chain IgLV3-21 Defines a New Poor Prognostic Subgroup in Chronic Lymphocytic Leukemia: Results of a Multicenter Study. *Clin Cancer Res*. 2018;24(20):5048-5057.

55.Wierz M, Pierson S, Gargiulo E, Guerin C, Moussay E, Paggetti J. Purification of Leukemia-Derived Exosomes to Study Microenvironment Modulation. *Methods Mol Biol*. 2019;1884:231-245.

56.Collot M, Ashokkumar P, Anton H, et al. MemBright: A Family of Fluorescent Membrane Probes for Advanced Cellular Imaging and Neuroscience. *Cell Chem Biol*. 2019;26(4):600-614 e607.

57.Thery C, Amigorena S, Raposo G, Clayton A. Isolation and characterization of exosomes from cell culture supernatants and biological fluids. *Curr Protoc Cell Biol*. 2006;Chapter 3:Unit 3 22.

58.Wang F, Li L, Piontek K, Sakaguchi M, Selaru FM. Exosome miR-335 as a novel therapeutic strategy in hepatocellular carcinoma. *Hepatology*. 2018;67(3):940-954.

59.Ioannou N, Hagner PR, Stokes M, et al. Triggering interferon signaling in T cells with avadomide sensitizes CLL to anti-PD-L1/PD-1 immunotherapy. *Blood*. 2021;137(2):216-231.

60.Robinson MD, McCarthy DJ, Smyth GK. edgeR: a Bioconductor package for differential expression analysis of digital gene expression data. *Bioinformatics*. 2010;26(1):139-140.

61.Tarazona S, Garcia-Alcalde F, Dopazo J, Ferrer A, Conesa A. Differential expression in RNA-seq: a matter of depth. *Genome Res*. 2011;21(12):2213-2223.

62.Meiser J, Schuster A, Pietzke M, et al. Increased formate overflow is a hallmark of oxidative cancer. *Nat Commun*. 2018;9(1):1368.

63.Ritchie ME, Phipson B, Wu D, et al. limma powers differential expression analyses for RNA-sequencing and microarray studies. *Nucleic Acids Res*. 2015;43(7):e47.

64.Nazarov PV, Wienecke-Baldacchino AK, Zinovyev A, et al. Deconvolution of transcriptomes and miRNomes by independent component analysis provides insights into biological processes and clinical outcomes of melanoma patients. *BMC Med Genomics*. 2019;12(1):132.

65.Coll-de la Rubia E, Martinez-Garcia E, Dittmar G, et al. In silico Approach for Validating and Unveiling New Applications for Prognostic Biomarkers of Endometrial Cancer. *Cancers (Basel)*. 2021;13(20).

## Figure legends

**Figure 1. Small EV are enriched in the human and murine leukemic microenvironments**

**(A)** Relative mRNA expression of selected genes involved in sEV biogenesis and secretion in B-cells from peripheral blood of healthy donors (HC, n=9) and CLL patients (CLL, n=15; from GSE67640). **(B)** Score based on sEV-related mRNA levels from panel A. **(C)** mRNA levels of selected genes extracted from panel A. **(D)** mRNA expression of selected genes according to IGHV mutational status. **(E)** Score combining the expression of *Rab10*, *Rab35*, and *Rab40C* according to IGHV mutational status **(F)** Relative mRNA expression of selected genes involved in sEV biogenesis and secretion in B-cells from C57BL/6 (WT) and Eµ-TCL1 mice (TCL1; from GSE175564). **(G)** Score based on sEV-related RNA levels from panel F. **(H)** *Rab3b* mRNA level extracted from panel F. **(I)** Detailed protocol to isolate and purify sEV from murine spleen. **(J)** Amount of proteins (in mg) recovered from LME- (n=18) or HCME-sEV (n=10), normalized per gram of spleen. **(K)** Representative TRPS analysis of ME-sEV for size and concentration. **(L)** Electron microscopy images of ME-sEV. **(M)** Western-blot analysis of ME-sEV. **(N)** HSNE clustering analysis of $MB488^+$ LME-sEV based on CD63, CD81 and CD9 expression measured by bead-free FC (left panel) and relative percentages of combined expression (right panel). $^*p<0.05$, $^{**}p<0.01$, $^{****}p<0.0001$ (unpaired Student *t* test). Data are mean.

**Figure 2. LME-sEV present a specific proteome and miRNA fingerprint**

**(A)** Hierarchical clustering of sEV differentially expressed proteins (DEP with q<0.05) identified by mass spectrometry between HCME-sEV (n=3, isolated from independent pools of 5 C57BL/6 spleens) and LME-sEV (n=14). **(B)** Volcano plot showing DEP between LME- and HCME-sEV with FDR<0.05 and $\log_2 FC>1$. **(C)** Principal Component (PC) analysis based on DEP. **(D-E)** Ontology analysis of DEP between LME-sEV and HCME-sEV. **(F)** Expression of ICP ligands on HCME- or LME-sEV quantified by bead-based FC. **(G)** Representative pictures of ICP ligand expression on single $MB488^+CD20^+$ LME-sEV visualized by imaging FC. **(H-I)** HSNE clustering of $MB488^+$ LME-sEV based on CD20, PD-L1, GAL9 and MHC-II expression analyzed by FC and related combinations of markers on $CD20^+$ LME-sEV. **(J)** miRNA levels measured using RT-qPCR from HCME- (isolated from a pool of 5 C57BL/6 mice spleens) and LME-sEV (n=8). Data are mean.

**Figure 3. LME-sEV enter different lymphocyte subsets and modify $CD8^+$ T-cells in the microenvironment**

**(A)** Percentage of splenocytes internalizing $MB488^+$ sEV. Splenocytes from C57BL/6 mice were incubated for increasing periods of time with $MB488^+$ LME-sEV, and analyzed by FC. Small EV pre-incubation with heparin sulfate (Hep) was performed for 4h. **(B)** Representative confocal microscopy pictures of total splenocytes after 4h of treatment with LME-sEV, in absence or presence of heparin. **(C)** Splenocytes from C57BL/6 mice were incubated for 24h with $MB488^+$ LME-sEV and then analyzed by FC with lymphocyte lineage markers. **(D)** FACS-sorted $CD4^+$ and $CD8^+$ T-cells were incubated for increasing periods of time with $MB488^+$ LME-sEV and analyzed by FC. **(E)** Representative confocal microscopy pictures of FACS-sorted $CD4^+$ $T_{conv}$ cells, $CD8^+$ T-cells and Tregs after treatment with LME-sEV (24h). **(F-H)** $MB570^+$-LME-sEV were i.v. injected in C57BL/6 mice. Total splenocytes were harvested 24h later and analyzed by FC directly (F) or after staining for specific immune subsets ($CD19^+$ B-cells, $CD4^+$ and $CD8^+$ T-cells, G-H). **(I)** Volcano plot showing DEG with FDR<0.05 and $\log_2 FC>1$ in $CD8^+$ T-cells isolated from spleens of mice treated with LME- or HCME-sEV for 1 week. **(J)** Hierarchical clustering of DEG from panel I. **(K)** t-distributed stochastic neighbor embedding (t-SNE) of samples from panel I. **(L)** Hierarchical clustering of selected genes from panel J, grouped by enriched gene ontologies. **(M-N)** mRNA (M) or protein levels (N) of 3 selected DEG from panel I, quantified by RT-qPCR or FC, in $CD8^+$ T-cells treated *in vitro* for 48h with HCME- or LME-sEV. $^*p<0.05$, $^{**}p<0.01$, $^{***}p<0.001$, $^{****}p<0.0001$ (unpaired Student *t* test). Data are mean.

### Figure 4. LME-sEV impact CD8$^+$ T-cell transcriptome, proteome and metabolome

**(A)** Volcano plot showing DEG identified by RNA-seq from CD8$^+$ T-cells treated for 48h with LME- (n=4) or HCME-sEV (n=3) with FDR<0.05 and $\log_2$FC>1. **(B-C)** Hierarchical clustering of all DEG (B) and of selected genes from relevant cell functions (C). **(D)** Volcano plot showing DEP identified by mass spectrometry from CD8$^+$ T -cells treated for 96h with LME- (n=3) and HCME-sEV (n=3) with FDR<0.05 and $\log_2$FC>1. **(E-F)** Gzmb mRNA expression and GzmB and perforin levels in CD8$^+$ T-cells treated for 48h with HCME- or LME-sEV. **(G-H)** Ontology analysis of enriched (G) or diminished (H) DEP in CD8$^+$ T-cells treated with LME- or HCME-sEV (from panel D). **(I)** Levels of glucose measured by mass spectrometry in culture medium in CD8$^+$ T-cell treated with LME- or HCME-sEV for 96h. Negative value represent consumption. **(J)** Immunoblot analysis of glycolysis-related proteins from CD8$^+$ T-cells treated for 96h with LME- or HCME-sEV. **(K)** Levels of ADP and ATP generated from $^{13}$C-glucose measured by mass spectrometry in CD8$^+$ T-cells treated with LME- (n=5) or HCME-sEV (n=6) for 96h. **(L)** Oxygen consumption measured by SeaHorse assay from CD8$^+$ T-cells treated with LME- or HCME-sEV for 96h. *p<0.05, **p<0.01, ****p<0.0001 (unpaired Student *t* test). Data are mean and SEM.

### Figure 5. LME-sEV decrease CD8$^+$ T-cell functions

**(A-B)** Percentages (A) and numbers (B) of CD62L$^-$KLRG1$^+$ CD8$^+$ T-cells after 48h of treatment with LME- and HCME-sEV assessed by FC. **(C)** Expression of ICP on CD62L$^-$KLRG1$^+$ CD8$^+$ T-cells from panel B. HSNE clustering depicting treatments, cluster identity and marker expression. **(D)** Hierarchical clustering based on ICP expression. **(E)** Percentages of PD1$^+$TIM3$^+$ICOS$^+$ CD8$^+$ T-cells from cluster C1 (upper panel) and of PD1$^+$LAG3$^+$TIM3$^+$TIGIT$^+$ICOS$^+$ CD8$^+$ T-cells from cluster C8 (lower panel). **(F-I)** CD8$^+$ T-cells were isolated from C57BL/6 and CLL cells from TCL1 mice. (F) Percentage of T-cell-mediated killing of TCL1 cells (cytotoxic assay) in presence of HCME-sEV or LME-sEV (N=6). (G) Quantification of CD8$^+$ T-cell:TCL1 cell conjugates upon treatment with LME- or HCME-sEV (N=3-4) and representative images (scale bar: 10 µm). (H) Quantification of immune synapse formation (F-actin area in µm$^2$, HCME, n=31 and LME-sEV, n=39, dashed line representing median) and representative medial optical sections (scale bar: 5 µm) with arrows indicating the synapse. (I) Mean Fluorescence Intensity (MFI) of GzmB at the synapse between CD8$^+$ T and CLL cells (HCME, n=31 and LME-sEV, n=51) and representative 3D volume-rendered images. **(J)** miRNA levels quantified by RT-qPCR in CD8$^+$ T-cells treated with HCME- or LME-sEV for 24h. **(K)** Protein levels of miRNA targets determined by FC in CD8$^+$ T-cells treated for 48h with HCME-sEV or LME-sEV transfected with scramble or antagomiRs (miR-150, -155 and -378a). Pre-incubation of LME-sEV with heparin was used as inhibitor of sEV internalization. **(L)** ICP levels determined by FC in CD8$^+$ T-cells treated for 48h with HCME-sEV or LME-sEV pre-incubated with blocking Abs (PD-L1, GAL9, VISTA and MHC-II) or corresponding isotypes. *p<0.05, **p<0.01, ***p<0.001, ****p<0.0001 (unpaired Student *t* test). Data are mean.

### Figure 6. Small EV are crucial for CLL development by impairing the anti-tumor immune response *in vivo*

**(A)** Generation of a new TCL1-RAB27DKO mouse model. **(B)** Detection of the human *TCL1* transgene and Rab27b excision in gDNA of C57BL/6, TCL1 and TCL1-RAB27DKO mice. **(C)** Immunoblot analysis of RAB27A and RAB27B proteins in the same mice. **(D)** Percentage of CD5$^+$CD19$^+$ CLL cells in the PB of TCL1 (n=35) or TCL1-RAB27DKO (n=12) mice over time. **(E)** Survival of mice from panel D and RAB27DKO mice (n=10). **(F)** Quantity of proteins recovered from LME-sEV (n=18) or LME-sEV $_{\text{TCL1-RAB27DKO}}$ (n=11) normalized per gram of spleen. **(G)** PCA based on DEP between LME-sEV$_{\text{TCL1-RAB27DKO}}$ and LME-sEV with FDR<0.05 and $\log_2$FC>1. **(H)** Volcano plot showing DEP. **(I)** Injection scheme of CLL cells competent (TCL1, red arrows) or deficient in sEV release (TCL1-RAB27DKO, green arrows) into C57BL/6 mice, with or without LME-sEV (violet arrows). **(J)** Percentage of CD5$^+$CD19$^+$ CLL cells in blood of C57BL/6 mice injected according to panel I (n=16 per condition). Four different clones for each genotype were injected in 4 mice each. **(K)** Injection scheme of

CLL cells deficient in sEV release (TCL1-RAB27DKO, green arrows) into C57BL/6 mice, treated with α-CD8 blocking or isotype control Abs (violet arrows). **(L)** Percentage of $CD5^+CD19^+$ CLL cells in the PB of mice injected according to panel K (n=6 per group) at day 14 and 21 (left panel) and in the spleen of the same mice at day 21. **(M)** Injection scheme of CLL cells deficient in sEV release (TCL1-RAB27DKO, green arrows) into C57BL/6 mice, together with α-CD8 blocking Ab (violet arrows) and followed by injection of activated $CD8^+$ T-cells treated *ex vivo* with HCME- (blue arrows) or LME-sEV (red arrows). **(N)** Percentage of $CD5^+CD19^+$ CLL cells at day 10 in the PB of mice injected according to panel M (n=4 per group). **(O)** Survival of mice from panel M (n=4 per group). *p<0.05, **p<0.01, ***p<0.001, ****p<0.0001 (unpaired Student *t* test for F, L, and N 2-way ANOVA followed by Bonferroni's multiple comparison test for D and J, log-Rank test for E and O). Data are mean with SEM.

**Figure 7: Expression of sEV-related genes correlates with disease progression and poor survival in CLL patients**

Gene expression analysis was performed by RT-qPCR for 7 genes involved in sEV biogenesis and secretion in a cohort of 144 CLL patients. The correlation between gene expression and survival was evaluated by Cox univariate regression analysis. Gene expression in clinical groups was evaluated by differential expression analysis for single genes or by logistic regression (LR) analysis for multiple genes. **(A)** Calculated hazard ratios >1 (red dots, p-value <0.05) indicate an increased risk for patients with high single-gene expression in term of overall survival (OS). **(B)** Correlation between high or low gene expression and OS. Low and High groups are of identical size (n=72) Median OS is indicated in months (mo). **(C)** Correlation between high or low combined 7-gene expression and OS. **(D)** Calculated hazard ratios >1 (red dots, p-value <0.05) indicate an increased risk for patients with high multiple gene expression in term of OS**.** **(E)** Calculated hazard ratios >1 (red dots, p-value <0.05) indicate an increased risk for patients with high single-gene expression in term of treatment-free survival (TFS). **(F)** Correlation between high or low gene expression and TFS. **(G-H)** Standardized expression of single genes (G) or logistic regression (LR) scores for multiple genes (H) in groups of patients according to prognostic markers (CytoG, cytogenetics, group size indicated in each panel). *p<0.05, **p<0.01. Data are mean with 95% confidence intervals.

# Figure 1

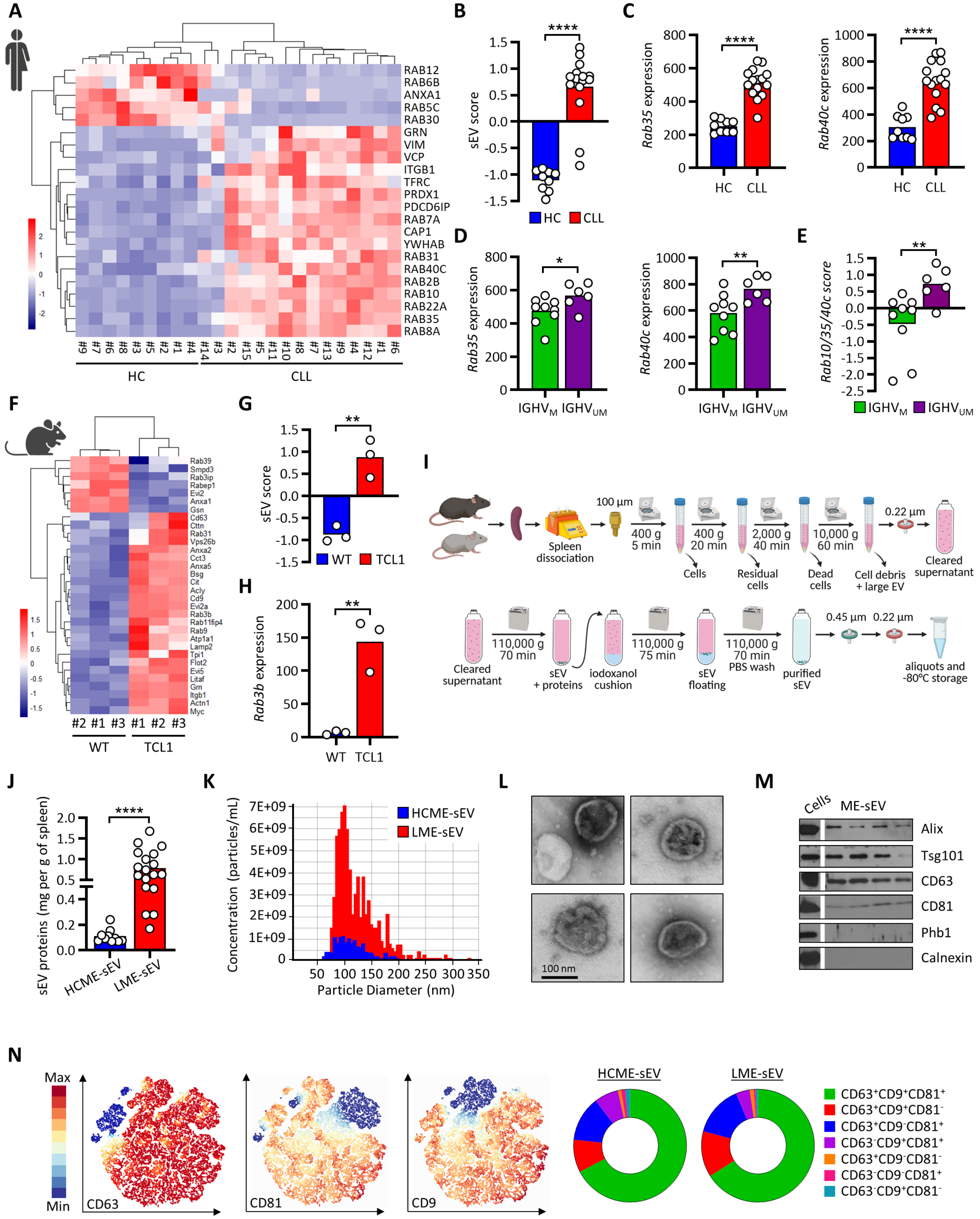
A
RAB12
RAB6B
ANXA1
RAB5C
RAB30
GRN
VIM
VCP
ITGB1
TFRC
PRDX1
PDCD6IP
RAB7A
CAP1
YWHAB
RAB31
RAB40C
RAB2B
RAB10
RAB22A
RAB35
RAB8A
2
1
0
-1
-2
#9 #7 #6 #8 #3 #5 #2 #1 #4 #14 #3 #2 #15 #5 #11 #10 #8 #7 #13 #9 #4 #12 #1 #6
HC
CLL
B
sEV score
1.5
1.0
0.5
0.0
-0.5
-1.0
-1.5
****
HC
CLL
C
Rab35 expression
800
600
400
200
0
****
HC CLL
Rab40c expression
1000
800
600
400
200
0
****
HC CLL
D
Rab35 expression
*
Rab40c expression
**
IGHV$_M$ IGHV$_{UM}$
E
Rab10/35/40c score
1.5
1.0
0.5
0.0
-0.5
-1.0
-1.5
-2.0
-2.5
**
IGHV$_M$
IGHV$_{UM}$
F
Rab39
Smpd3
Rab3ip
Rabep1
Evi2
Anxa1
Gsn
Cd63
Cttn
Rab31
Vps26b
Anxa2
Cct3
Anxa5
Bsg
Cit
Acly
Cd9
Evi2a
Rab3b
Rab11fip4
Rab9
Atp1a1
Lamp2
Tpi1
Flot2
Evi5
Litaf
Grn
Itgb1
Actn1
Myc
1.5
1
0.5
0
-0.5
-1
-1.5
#2 #1 #3 #1 #2 #3
WT
TCL1
G
sEV score
**
WT
TCL1
H
Rab3b expression
200
150
100
50
0
**
WT TCL1
I
Spleen dissociation
100 µm
400 g 5 min
400 g 20 min
2,000 g 40 min
10,000 g 60 min
0.22 µm
Cells
Residual cells
Dead cells
Cell debris + large EV
Cleared supernatant
Cleared supernatant
110,000 g 70 min
sEV + proteins
iodoxanol cushion
110,000 g 75 min
sEV floating
110,000 g 70 min PBS wash
purified sEV
0.45 µm
0.22 µm
aliquots and -80°C storage
J
sEV proteins (mg per g of spleen)
2.0
1.5
1.0
0.5
0.4
0.2
0.0
****
HCME-sEV
LME-sEV
K
Concentration (particles/mL)
7E+09
6E+09
5E+09
4E+09
3E+09
2E+09
1E+09
0
50 100 150 200 250 300 350
Particle Diameter (nm)
HCME-sEV
LME-sEV
L
100 nm
M
Cells
ME-sEV
Alix
Tsg101
CD63
CD81
Phb1
Calnexin
N
Max
Min
CD63
CD81
CD9
HCME-sEV
LME-sEV
CD63$^+$CD9$^+$CD81$^+$
CD63$^+$CD9$^+$CD81$^-$
CD63$^+$CD9$^-$CD81$^+$
CD63$^-$CD9$^+$CD81$^+$
CD63$^+$CD9$^-$CD81$^-$
CD63$^-$CD9$^-$CD81$^+$
CD63$^-$CD9$^+$CD81$^-$

# Figure 2

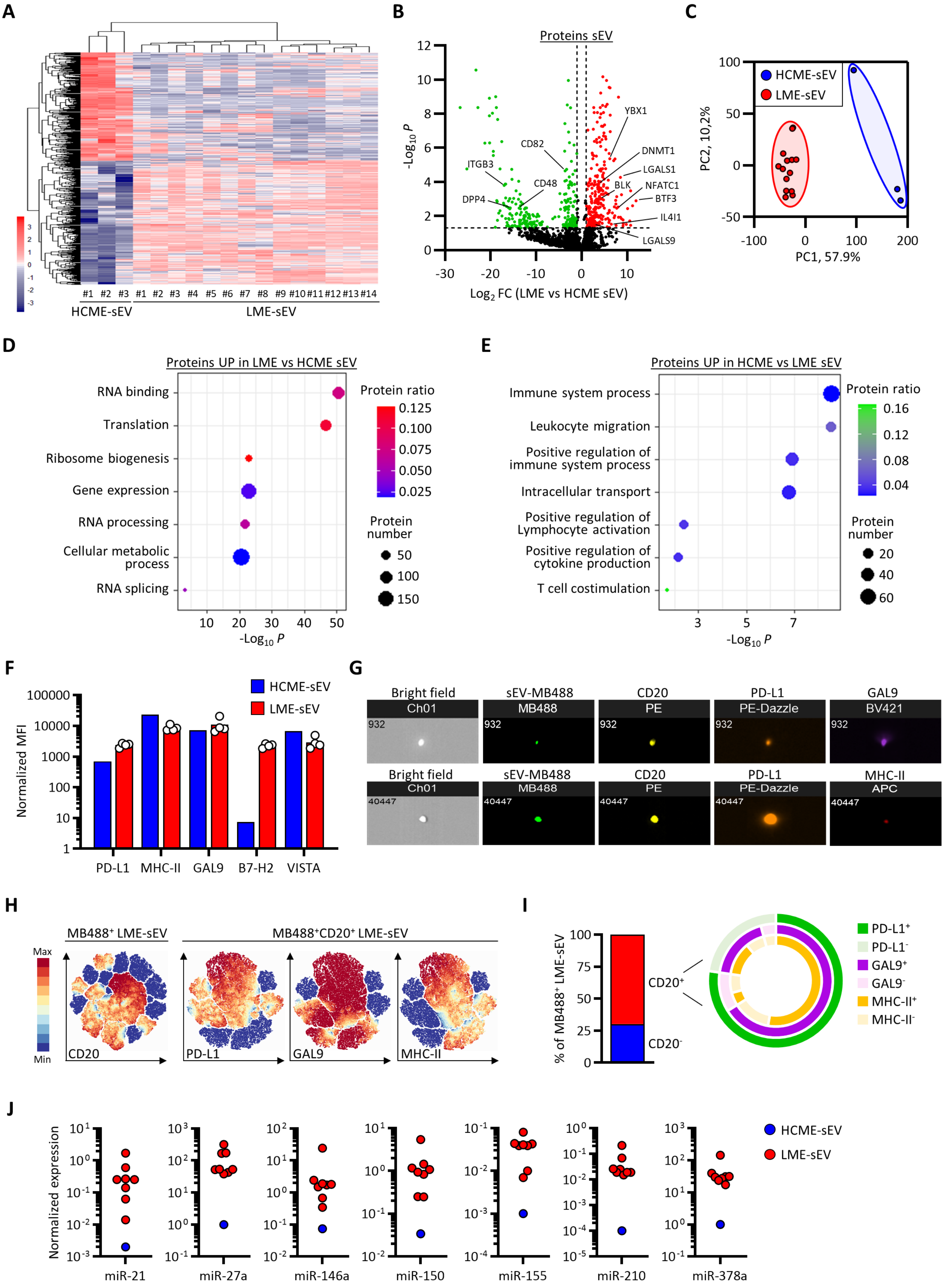
A
#1 #2 #3 #1 #2 #3 #4 #5 #6 #7 #8 #9 #10 #11 #12 #13 #14
HCME-sEV
LME-sEV
3 2 1 0 -1 -2 -3
B
Proteins sEV
$-\text{Log}_{10}\,P$
$\text{Log}_2$ FC (LME vs HCME sEV)
YBX1
DNMT1
LGALS1
BLK
NFATC1
BTF3
IL4I1
LGALS9
CD82
ITGB3
CD48
DPP4
C
HCME-sEV
LME-sEV
PC2, 10,2%
PC1, 57.9%
D
Proteins UP in LME vs HCME sEV
RNA binding
Translation
Ribosome biogenesis
Gene expression
RNA processing
Cellular metabolic process
RNA splicing
$-\text{Log}_{10}\,P$
Protein ratio
0.125
0.100
0.075
0.050
0.025
Protein number
50
100
150
E
Proteins UP in HCME vs LME sEV
Immune system process
Leukocyte migration
Positive regulation of immune system process
Intracellular transport
Positive regulation of Lymphocyte activation
Positive regulation of cytokine production
T cell costimulation
$-\text{Log}_{10}\,P$
Protein ratio
0.16
0.12
0.08
0.04
Protein number
20
40
60
F
HCME-sEV
LME-sEV
Normalized MFI
PD-L1
MHC-II
GAL9
B7-H2
VISTA
G
Bright field
Ch01
sEV-MB488
MB488
CD20
PE
PD-L1
PE-Dazzle
GAL9
BV421
MHC-II
APC
932
40447
H
MB488⁺ LME-sEV
MB488⁺CD20⁺ LME-sEV
Max
Min
CD20
PD-L1
GAL9
MHC-II
I
% of MB488⁺ LME-sEV
CD20⁺
CD20⁻
PD-L1⁺
PD-L1⁻
GAL9⁺
GAL9⁻
MHC-II⁺
MHC-II⁻
J
Normalized expression
miR-21
miR-27a
miR-146a
miR-150
miR-155
miR-210
miR-378a
HCME-sEV
LME-sEV

**Figure 3**

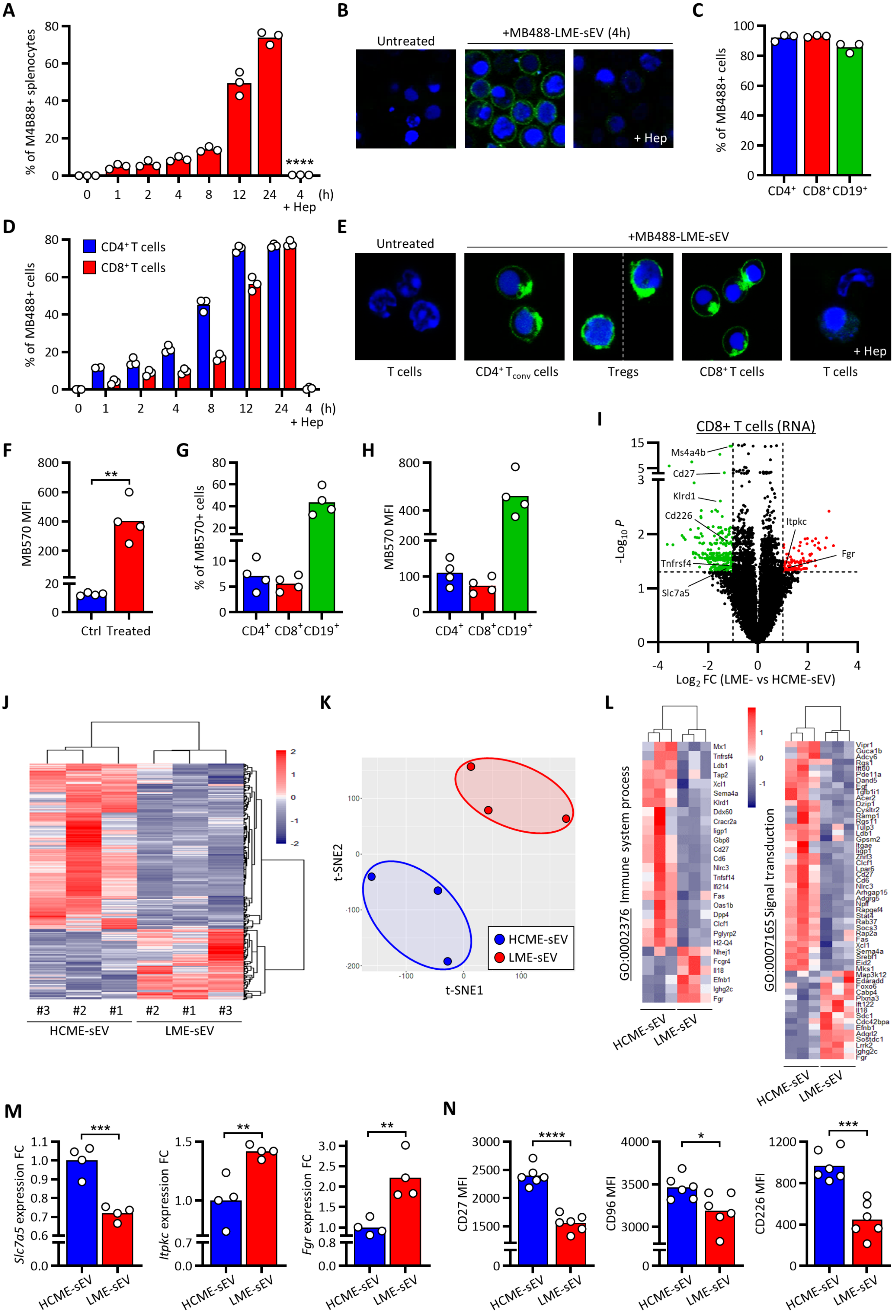
A
% of M4B88+ splenocytes
0
20
40
60
80
0
1
2
4
8
12
24
4
+ Hep
(h)
****
B
Untreated
+MB488-LME-sEV (4h)
+ Hep
C
% of MB488+ cells
0
20
40
60
80
100
CD4+
CD8+
CD19+
D
% of MB488+ cells
CD4+ T cells
CD8+ T cells
0
20
40
60
80
0
1
2
4
8
12
24
4
+ Hep
(h)
E
Untreated
+MB488-LME-sEV
+ Hep
T cells
CD4+ Tconv cells
Tregs
CD8+ T cells
T cells
F
MB570 MFI
0
20
200
400
600
800
**
Ctrl
Treated
G
% of MB570+ cells
0
5
10
20
40
60
80
CD4+
CD8+
CD19+
H
MB570 MFI
0
100
200
400
800
CD4+
CD8+
CD19+
I
CD8+ T cells (RNA)
-Log10 P
0
1
2
3
5
15
Log2 FC (LME- vs HCME-sEV)
-4
-2
0
2
4
Ms4a4b
Cd27
Klrd1
Cd226
Tnfrsf4
Slc7a5
Itpkc
Fgr
J
2
1
0
-1
-2
#3
#2
#1
#2
#1
#3
HCME-sEV
LME-sEV
K
t-SNE2
t-SNE1
100
0
-100
-200
-100
0
100
HCME-sEV
LME-sEV
L
GO:0002376 Immune system process
1
0
-1
Mx1
Tnfrsf4
Ldb1
Tap2
Xcl1
Sema4a
Klrd1
Ddx60
Cracr2a
Iigp1
Gbp8
Cd27
Cd6
Nlrc3
Tnfsf14
Ifi214
Fas
Oas1b
Dpp4
Clcf1
Pglyrp2
H2-Q4
Nhej1
Fcgr4
Il18
Efnb1
Ighg2c
Fgr
HCME-sEV
LME-sEV
GO:0007165 Signal transduction
Vipr1
Guca1b
Adcy6
Rgs1
Ift80
Pde11a
Dand5
Egf
Tgfb1i1
Acer2
Dzip1
Cysltr2
Ramp1
Rgs11
Tulp3
Ldb1
Gpsm2
Itgae
Iigp1
Znrf3
Clcf1
Lpar6
Cd27
Cd6
Nlrc3
Arhgap15
Adgrg5
Npff
Rapgef4
Stat4
Rab37
Socs3
Rap2a
Fas
Xcl1
Sema4a
Srebf1
Eid2
Mks1
Map3k12
Edaradd
Foxo6
Cabp4
Plxna3
Ift122
Il18
Sdc1
Cdc42bpa
Efnb1
Adgrl2
Sostdc1
Lrrk2
Ighg2c
Fgr
HCME-sEV
LME-sEV
M
Slc7a5 expression FC
0.0
0.6
0.7
0.8
0.9
1.0
1.1
***
Itpkc expression FC
0.0
0.7
1.0
1.5
**
Fgr expression FC
0.0
0.8
1.0
1.5
2.0
2.5
3.0
**
HCME-sEV
LME-sEV
N
CD27 MFI
0
1500
2000
2500
3000
****
CD96 MFI
0
3000
3500
4000
*
CD226 MFI
0
400
800
1200
***
HCME-sEV
LME-sEV

# Figure 4

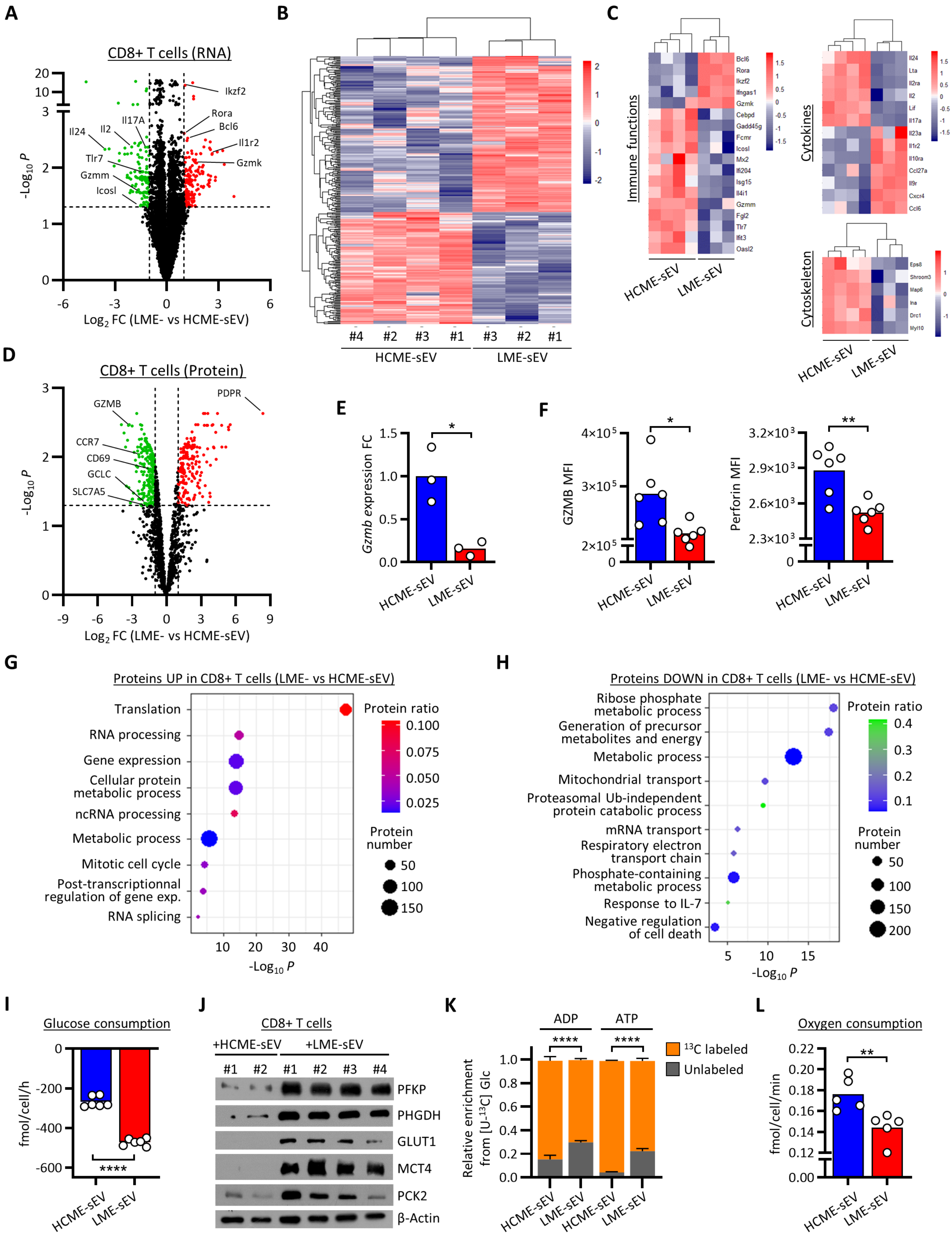
A
CD8+ T cells (RNA)
-Log10 P
Log2 FC (LME- vs HCME-sEV)
Ikzf2
Rora
Bcl6
Il1r2
Gzmk
Il24
Il2
Il17A
Tlr7
Gzmm
Icosl
B
#4
#2
#3
#1
#3
#2
#1
HCME-sEV
LME-sEV
C
Immune functions
Bcl6
Rora
Ikzf2
Ifngas1
Gzmk
Cebpd
Gadd45g
Fcmr
Icosl
Mx2
Ifi204
Isg15
Il4i1
Gzmm
Fgl2
Tlr7
Ifit3
Oasl2
Cytokines
Il24
Lta
Il2ra
Il2
Lif
Il17a
Il23a
Il1r2
Il10ra
Ccl27a
Il9r
Cxcr4
Ccl6
Cytoskeleton
Eps8
Shroom3
Map6
Ina
Drc1
Myl10
HCME-sEV
LME-sEV
D
CD8+ T cells (Protein)
-Log10 P
Log2 FC (LME- vs HCME-sEV)
PDPR
GZMB
CCR7
CD69
GCLC
SLC7A5
E
Gzmb expression FC
HCME-sEV
LME-sEV
*
F
GZMB MFI
Perforin MFI
*
**
HCME-sEV
LME-sEV
G
Proteins UP in CD8+ T cells (LME- vs HCME-sEV)
Translation
RNA processing
Gene expression
Cellular protein metabolic process
ncRNA processing
Metabolic process
Mitotic cell cycle
Post-transcriptionnal regulation of gene exp.
RNA splicing
-Log10 P
Protein ratio
Protein number
H
Proteins DOWN in CD8+ T cells (LME- vs HCME-sEV)
Ribose phosphate metabolic process
Generation of precursor metabolites and energy
Metabolic process
Mitochondrial transport
Proteasomal Ub-independent protein catabolic process
mRNA transport
Respiratory electron transport chain
Phosphate-containing metabolic process
Response to IL-7
Negative regulation of cell death
-Log10 P
Protein ratio
Protein number
I
Glucose consumption
fmol/cell/h
****
HCME-sEV
LME-sEV
J
CD8+ T cells
+HCME-sEV
+LME-sEV
#1
#2
#1
#2
#3
#4
PFKP
PHGDH
GLUT1
MCT4
PCK2
β-Actin
K
ADP
ATP
****
****
13C labeled
Unlabeled
Relative enrichment from [U-13C] Glc
HCME-sEV
LME-sEV
HCME-sEV
LME-sEV
L
Oxygen consumption
fmol/cell/min
**
HCME-sEV
LME-sEV

# Figure 5

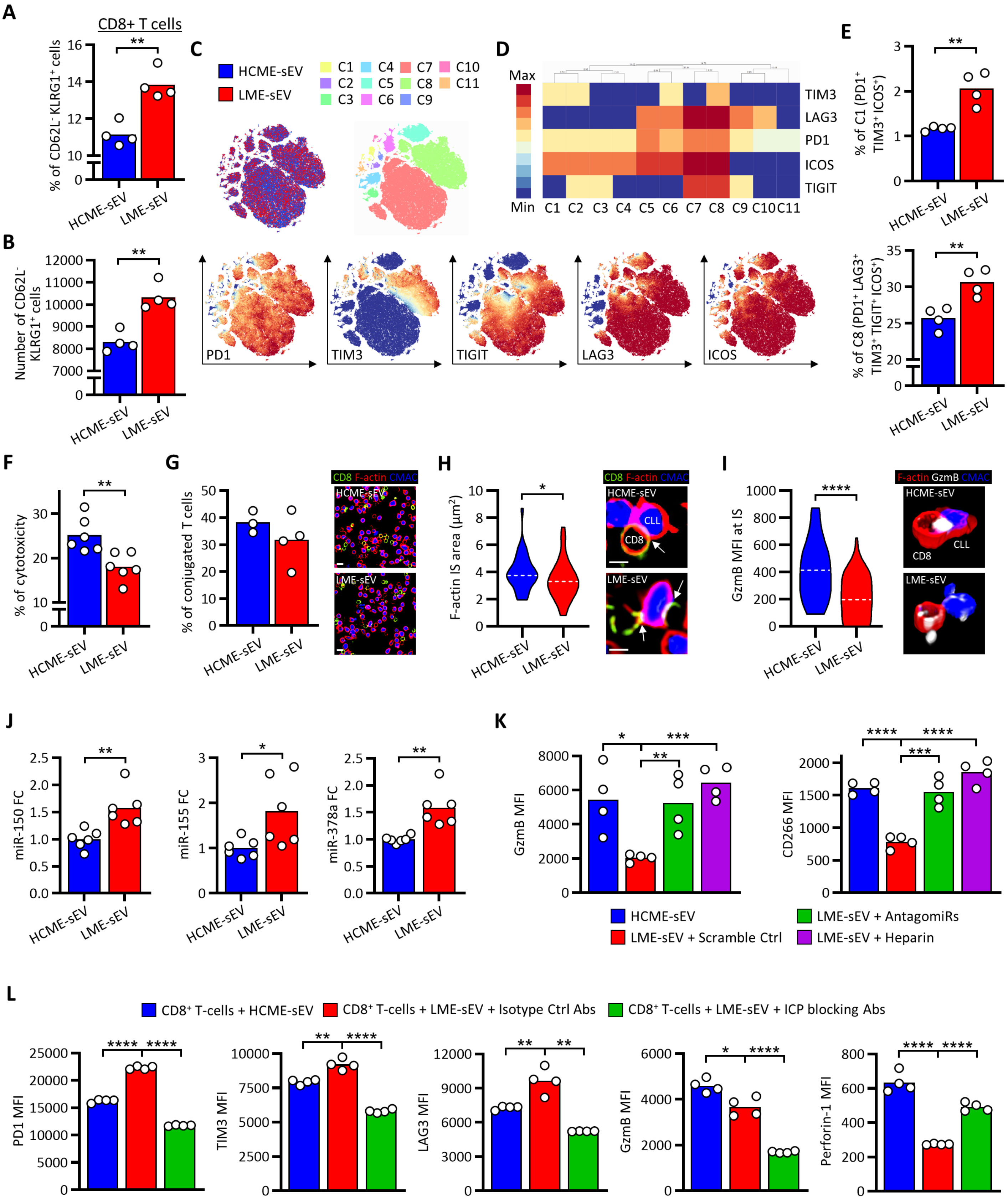
A
CD8+ T cells
% of CD62L⁻ KLRG1⁺ cells
16
14
12
10
0
**
HCME-sEV
LME-sEV
B
Number of CD62L⁻ KLRG1⁺ cells
12000
11000
10000
9000
8000
7000
0
**
HCME-sEV
LME-sEV
C
HCME-sEV
LME-sEV
C1
C2
C3
C4
C5
C6
C7
C8
C9
C10
C11
PD1
TIM3
TIGIT
LAG3
ICOS
D
Max
Min
C1 C2 C3 C4 C5 C6 C7 C8 C9 C10 C11
TIM3
LAG3
PD1
ICOS
TIGIT
E
% of C1 (PD1⁺ TIM3⁺ ICOS⁺)
3
2
1
0
**
HCME-sEV
LME-sEV
% of C8 (PD1⁺ LAG3⁺ TIM3⁺ TIGIT⁺ ICOS⁺)
35
30
25
20
0
**
HCME-sEV
LME-sEV
F
% of cytotoxicity
30
20
10
0
**
HCME-sEV
LME-sEV
G
% of conjugated T cells
50
40
30
20
10
0
HCME-sEV
LME-sEV
CD8 F-actin CMAC
HCME-sEV
LME-sEV
H
F-actin IS area (µm²)
10
8
6
4
2
0
*
HCME-sEV
LME-sEV
CD8 F-actin CMAC
HCME-sEV
CLL
CD8
LME-sEV
I
GzmB MFI at IS
1000
800
600
400
200
0
****
HCME-sEV
LME-sEV
F-actin GzmB CMAC
HCME-sEV
CLL
CD8
LME-sEV
J
miR-150 FC
2.5
2.0
1.5
1.0
0.5
0.0
**
HCME-sEV
LME-sEV
miR-155 FC
3
2
1
0
*
HCME-sEV
LME-sEV
miR-378a FC
2.5
2.0
1.5
1.0
0.5
0.0
**
HCME-sEV
LME-sEV
K
GzmB MFI
8000
6000
4000
2000
0
*
***
**
CD266 MFI
2000
1500
1000
500
0
****
****
***
HCME-sEV
LME-sEV + Scramble Ctrl
LME-sEV + AntagomiRs
LME-sEV + Heparin
L
CD8⁺ T-cells + HCME-sEV
CD8⁺ T-cells + LME-sEV + Isotype Ctrl Abs
CD8⁺ T-cells + LME-sEV + ICP blocking Abs
PD1 MFI
25000
20000
15000
10000
5000
0
**** ****
TIM3 MFI
10000
7500
5000
2500
0
** ****
LAG3 MFI
12000
9000
6000
3000
0
** **
GzmB MFI
6000
4000
2000
0
* ****
Perforin-1 MFI
800
600
400
200
0
**** ****

# Figure 6

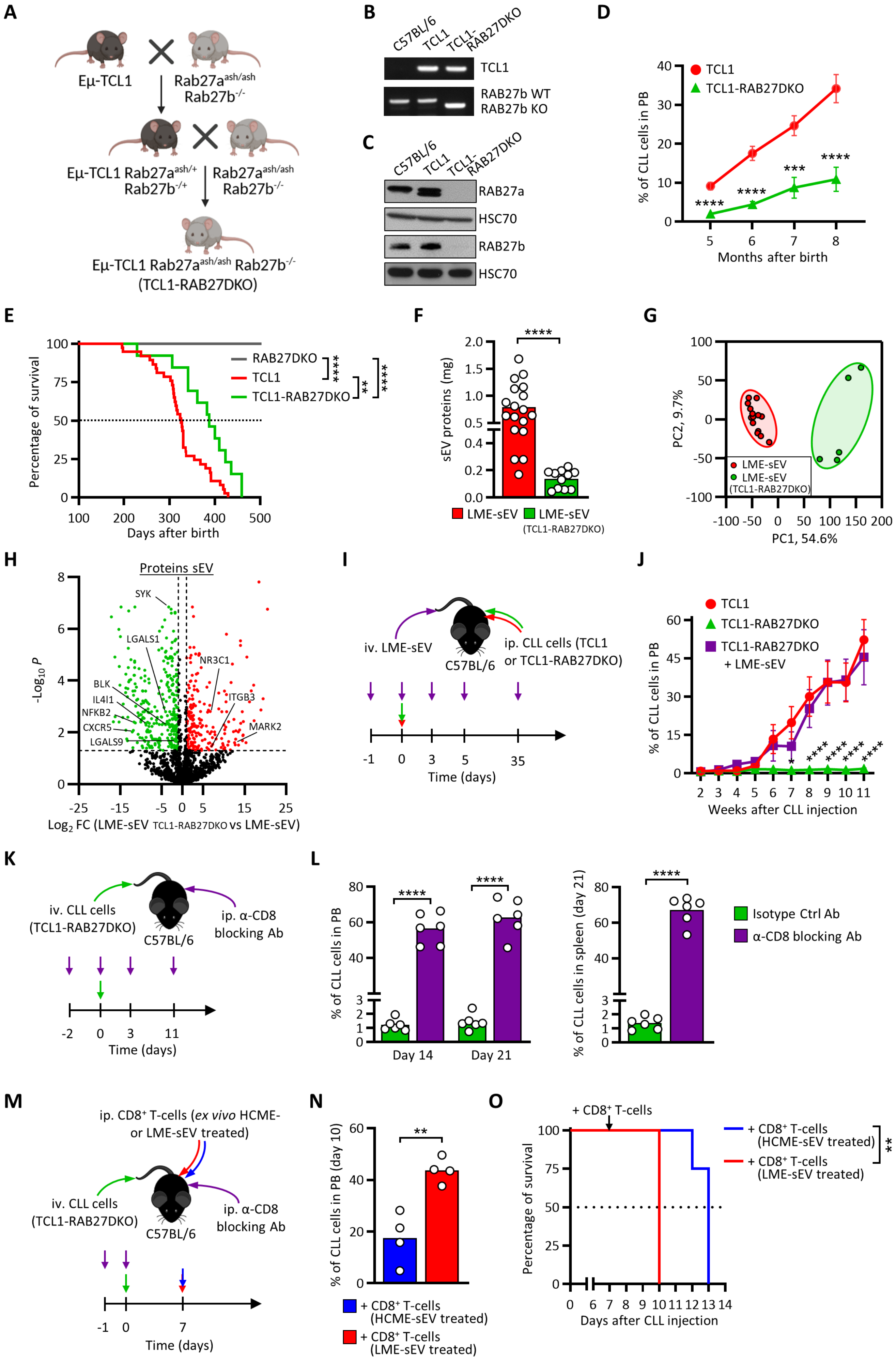
A
Eμ-TCL1
Rab27a$^{ash/ash}$ Rab27b$^{-/-}$
Eμ-TCL1 Rab27a$^{ash/+}$ Rab27b$^{-/+}$
Rab27a$^{ash/ash}$ Rab27b$^{-/-}$
Eμ-TCL1 Rab27a$^{ash/ash}$ Rab27b$^{-/-}$
(TCL1-RAB27DKO)
B
C57BL/6
TCL1
TCL1-RAB27DKO
TCL1
RAB27b WT
RAB27b KO
C
C57BL/6
TCL1
TCL1-RAB27DKO
RAB27a
HSC70
RAB27b
HSC70
D
TCL1
TCL1-RAB27DKO
% of CLL cells in PB
Months after birth
****
****
***
****
E
RAB27DKO
TCL1
TCL1-RAB27DKO
****
**
****
Percentage of survival
Days after birth
F
sEV proteins (mg)
****
LME-sEV
LME-sEV (TCL1-RAB27DKO)
G
PC2, 9.7%
PC1, 54.6%
LME-sEV
LME-sEV (TCL1-RAB27DKO)
H
Proteins sEV
SYK
LGALS1
BLK
IL4I1
NFKB2
CXCR5
LGALS9
NR3C1
ITGB3
MARK2
$-Log_{10} P$
$Log_2$ FC (LME-sEV TCL1-RAB27DKO vs LME-sEV)
I
iv. LME-sEV
C57BL/6
ip. CLL cells (TCL1 or TCL1-RAB27DKO)
Time (days)
J
TCL1
TCL1-RAB27DKO
TCL1-RAB27DKO + LME-sEV
% of CLL cells in PB
Weeks after CLL injection
*
****
K
iv. CLL cells (TCL1-RAB27DKO)
C57BL/6
ip. α-CD8 blocking Ab
Time (days)
L
****
% of CLL cells in PB
Day 14
Day 21
% of CLL cells in spleen (day 21)
Isotype Ctrl Ab
α-CD8 blocking Ab
M
ip. CD8⁺ T-cells (ex vivo HCME- or LME-sEV treated)
iv. CLL cells (TCL1-RAB27DKO)
C57BL/6
ip. α-CD8 blocking Ab
Time (days)
N
**
% of CLL cells in PB (day 10)
+ CD8⁺ T-cells (HCME-sEV treated)
+ CD8⁺ T-cells (LME-sEV treated)
O
+ CD8⁺ T-cells
Percentage of survival
Days after CLL injection
+ CD8⁺ T-cells (HCME-sEV treated)
+ CD8⁺ T-cells (LME-sEV treated)
**

## Figure 7

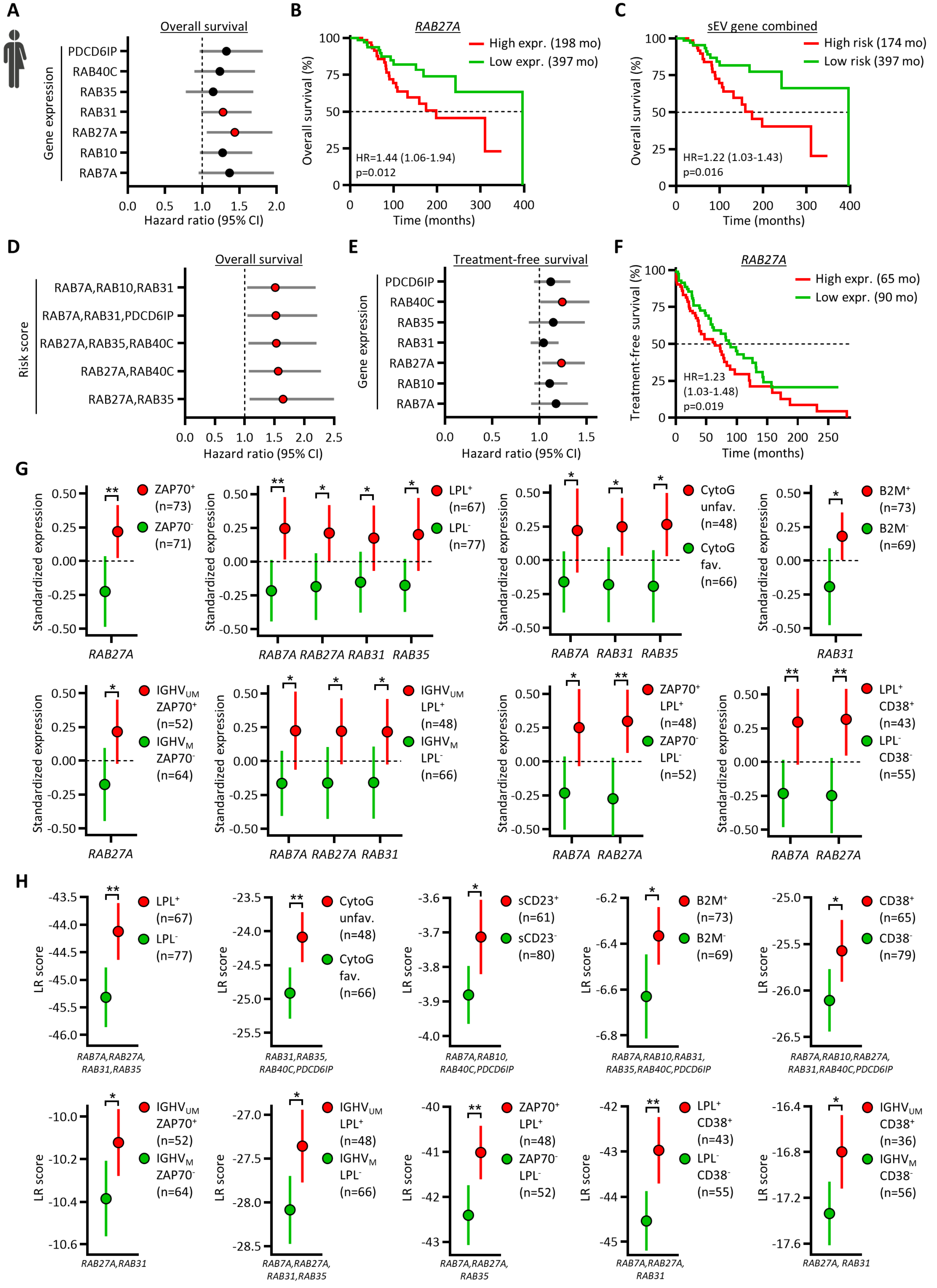
A
Overall survival
Gene expression
PDCD6IP
RAB40C
RAB35
RAB31
RAB27A
RAB10
RAB7A
0.0 0.5 1.0 1.5 2.0
Hazard ratio (95% CI)
B
*RAB27A*
High expr. (198 mo)
Low expr. (397 mo)
Overall survival (%)
HR=1.44 (1.06-1.94)
p=0.012
Time (months)
C
sEV gene combined
High risk (174 mo)
Low risk (397 mo)
Overall survival (%)
HR=1.22 (1.03-1.43)
p=0.016
Time (months)
D
Overall survival
Risk score
RAB7A,RAB10,RAB31
RAB7A,RAB31,PDCD6IP
RAB27A,RAB35,RAB40C
RAB27A,RAB40C
RAB27A,RAB35
0.0 0.5 1.0 1.5 2.0 2.5
Hazard ratio (95% CI)
E
Treatment-free survival
Gene expression
PDCD6IP
RAB40C
RAB35
RAB31
RAB27A
RAB10
RAB7A
0.0 0.5 1.0 1.5
Hazard ratio (95% CI)
F
*RAB27A*
High expr. (65 mo)
Low expr. (90 mo)
Treatment-free survival (%)
HR=1.23
(1.03-1.48)
p=0.019
Time (months)
G
Standardized expression
ZAP70⁺ (n=73)
ZAP70⁻ (n=71)
*RAB27A*
LPL⁺ (n=67)
LPL⁻ (n=77)
*RAB7A* *RAB27A* *RAB31* *RAB35*
CytoG unfav. (n=48)
CytoG fav. (n=66)
*RAB7A* *RAB31* *RAB35*
B2M⁺ (n=73)
B2M⁻ (n=69)
*RAB31*
IGHV_UM ZAP70⁺ (n=52)
IGHV_M ZAP70⁻ (n=64)
*RAB27A*
IGHV_UM LPL⁺ (n=48)
IGHV_M LPL⁻ (n=66)
*RAB7A* *RAB27A* *RAB31*
ZAP70⁺ LPL⁺ (n=48)
ZAP70⁻ LPL⁻ (n=52)
*RAB7A* *RAB27A*
LPL⁺ CD38⁺ (n=43)
LPL⁻ CD38⁻ (n=55)
*RAB7A* *RAB27A*
H
LR score
LPL⁺ (n=67)
LPL⁻ (n=77)
*RAB7A,RAB27A, RAB31,RAB35*
CytoG unfav. (n=48)
CytoG fav. (n=66)
*RAB31,RAB35, RAB40C,PDCD6IP*
sCD23⁺ (n=61)
sCD23⁻ (n=80)
*RAB7A,RAB10, RAB40C,PDCD6IP*
B2M⁺ (n=73)
B2M⁻ (n=69)
*RAB7A,RAB10,RAB31, RAB35,RAB40C,PDCD6IP*
CD38⁺ (n=65)
CD38⁻ (n=79)
*RAB7A,RAB10,RAB27A, RAB31,RAB40C,PDCD6IP*
IGHV_UM ZAP70⁺ (n=52)
IGHV_M ZAP70⁻ (n=64)
*RAB27A,RAB31*
IGHV_UM LPL⁺ (n=48)
IGHV_M LPL⁻ (n=66)
*RAB7A,RAB27A, RAB31,RAB35*
ZAP70⁺ LPL⁺ (n=48)
ZAP70⁻ LPL⁻ (n=52)
*RAB7A,RAB27A, RAB35*
LPL⁺ CD38⁺ (n=43)
LPL⁻ CD38⁻ (n=55)
*RAB7A,RAB27A, RAB31*
IGHV_UM CD38⁺ (n=36)
IGHV_M CD38⁻ (n=56)
*RAB27A, RAB31*